Dynamical structure factors and excitation modes of the bilayer Heisenberg model

M. Lohöfer,[1] T. Coletta,[2] D. G. Joshi,[3] F. F. Assaad,[4] M. Vojta,[3] S. Wessel,[1] and F. Mila[5]

[1]*Institut für Theoretische Festkörperphysik, JARA-FIT and JARA-HPC, RWTH Aachen University, 52056 Aachen, Germany*

[2]*School of Engineering, University of Applied Sciences of Western Switzerland, 1951 Sion, Switzerland*

[3]*Institut für Theoretische Physik, Technische Universität Dresden, 01062 Dresden, Germany*

[4]*Institut für Theoretische Physik und Astrophysik, Universität Würzburg, Am Hubland, 97074 Würzburg, Germany*

[5]*Institute of Theoretical Physics, Ecole Polytechnique Fédérale de Lausanne (EPFL), 1015 Lausanne, Switzerland*

(Received 4 September 2015; published 29 December 2015)

Using quantum Monte Carlo simulations along with higher-order spin-wave theory, bond-operator and strong-coupling expansions, we analyze the dynamical spin structure factor of the spin-half Heisenberg model on the square-lattice bilayer. We identify distinct contributions from the low-energy Goldstone modes in the magnetically ordered phase and the gapped triplon modes in the quantum disordered phase. In the antisymmetric (with respect to layer inversion) channel, the dynamical spin structure factor exhibits a continuous evolution of spectral features across the quantum phase transition, connecting the two types of modes. Instead, in the symmetric channel, we find a depletion of the spectral weight when moving from the ordered to the disordered phase. While the dynamical spin structure factor does not exhibit a well-defined distinct contribution from the amplitude (or Higgs) mode in the ordered phase, we identify an only marginally damped amplitude mode in the dynamical singlet structure factor, obtained from interlayer bond correlations, in the vicinity of the quantum critical point. These findings provide quantitative information in direct relation to possible neutron or light scattering experiments in a fundamental two-dimensional quantum-critical spin system.

DOI: 10.1103/PhysRevB.92.245137 PACS number(s): 75.10.Jm, 75.40.Gb, 74.40.Kb, 75.40.Mg

I. INTRODUCTION

Advances in both energy and angular resolution of scattering experiments enable refined experimental studies of collective excitations in strongly correlated quantum many-body systems. A prominent example is the three-dimensional quantum spin-dimer system $TlCuCl_3$ where spin excitations have been mapped out in great detail using inelastic neutron scattering [1,2]. This compound exhibits a pressure-tuned zero-temperature transition from a gapped quantum disordered phase to an antiferromagnetically ordered phase. In addition to identifying the low-energy (transverse) Goldstone modes that accompany the spontaneous breaking of spin-rotation symmetry in the ordered phase, neutron scattering also detected the gapped (longitudinal) amplitude mode of the order-parameter field, frequently referred to as Higgs mode. In the three-dimensional compound $TlCuCl_3$, a rather successful quantitative theoretical account of these various spin excitation modes and the experimentally determined spectral weight can be obtained within a bond-operator mean-field description. In fact, the critical theory describing the underlying quantum critical point is the classical O(3) field theory in four dimensions, which exhibits only logarithmic corrections to a Gaussian fixed point. This fact also implies that for nearly critical three-dimensional collinear antiferromagnets, the amplitude mode becomes increasingly sharp upon approaching the quantum critical point [3].

Upon lowering the dimensionality of the quantum magnet, however, the effects of both thermal and quantum fluctuations get significantly enhanced. In particular, for two-dimensional Heisenberg systems, true long-range order is restricted to zero temperature, and the quantum phase transition of spin-dimer models is controlled by the classical Wilson-Fisher fixed point in three dimensions where interactions are relevant [4]. These interactions influence the visibility of the amplitude mode, as it can efficiently decay into pairs of Goldstone bosons. This has been examined intensively in recent years, with a focus towards U(1)-symmetric systems such as superconductors or ultracold atom gases in optical lattices [5–11]. It has been concluded from analyzing both microscopic models and order-parameter field theories that the amplitude mode will be strongly masked, due to damping, in the order-parameter correlation function. However, a distinct signal of the amplitude mode can be isolated from accessing the so-called scalar susceptibility, in terms of correlations of the squared order-parameter field. For magnetic systems, such as the one under consideration here, this implies that the amplitude mode, while not directly visible in the dynamical spin structure factor, should be accessible via appropriate scalar correlation functions, e.g., of bond-based spin-singlet operators [5,13]. The feasibility of using probes coupling to singlet observables in order to detect the amplitude mode in (three-dimensional) magnets, e.g. via light scattering, has recently been considered also within bond-operator mean-field theory [14,15]. From field-theoretical arguments it is expected that a marginally damped amplitude mode may be detected in close vicinity of the quantum critical point, while deep in the ordered regime it merges with the continuum of multimagnon excitations, which exhibits a diverging spectrum (e.g., scaling as $\sim 1/\omega$ with the frequency ω at the ordering wave vector [16]), masking the amplitude mode. While such general conclusions may be drawn based on field-theory considerations, it is of genuine interest—also for future experimental probes—to provide more quantitative microscopic details on the excitation spectra of two-dimensional quantum magnets across quantum critical points.

In this paper, we use quantum Monte Carlo simulations combined with a stochastic analytic continuation approach to access the dynamical spin structure factor and adequate scalar response functions for the spin-half quantum Heisenberg model on the two-dimensional square-lattice bilayer. This model has been established [17–23] as a basic spin model

exhibiting a quantum critical point: as a function of the ratio $g = J'/J$ between the interlayer (J') to the intralayer (J) exchange coupling, it exhibits a quantum phase transition at a critical ratio [23] $g_c = 2.5220(1)$ that separates the small-g collinear antiferromagnet from the large-g quantum disordered dimer paramagnet. This model has been analysed rather intensively in the past, and in particular, large-scale quantum Monte Carlo simulations have identified both the above quoted location of the quantum critical point and verified the three-dimensional O(3) universality class of the quantum phase transition. In fact, due to the absence of geometric frustration, this system can be studied using quantum Monte Carlo without any sign problem, even in close vicinity of the quantum critical point, by using by-now standard cluster update algorithms. More recently, using an extended ensemble approach, also the quantum entanglement properties across the quantum phase transition have been analysed and possible universal contributions in the bipartite entanglement have been identified [24].

However, no detailed account on dynamical properties based on quantum Monte Carlo simulations has been provided thus far. Clearly, detecting the characteristic excitation modes of both phases in realistic spectral probes is of most interest here. To access such dynamical properties based on quantum Monte Carlo simulations, one requires high-quality statistical data in order to perform the analytic continuation from the imaginary-time quantum Monte Carlo data to real frequencies. We note that dispersion relations of the excitation modes have been studied previously, based on various analytical approaches such as bond-operator mean-field theory or series expansions [22,25]. However, a more direct relation to experimental probes requires also a quantitative evaluation of the spectral-weight distribution. In that respect, one of the fundamental questions is how one crosses over from two gapless spin-wave excitations in the limit of weakly coupled planes to gapped triplon [26] excitations at strong interplane coupling. This issue is of experimental relevance as well. For instance, the material $BaCuSi_2O_6$ is believed to realize [27–29] the spin-half bilayer Heisenberg model on the square lattice (interactions between the bilayers are weak and frustrated). These results are also expected to be of interest in the discussion of the bilayer iridate $Sr_3Ir_2O_7$ [30,31].

In the following, we provide a detailed account on the spectral-weight distribution in the dynamical spin structure factor and also address the detection of the amplitude mode by appropriate scalar response functions. The paper is organised as follows. In Sec. II, we introduce the model Hamiltonian and the used computational and analytical methods. The dynamical spin structure factor of the bilayer model is then analysed in Sec. III, while Sec. IV concentrates on the detection of the amplitude mode. The results of our analysis are summarised in the concluding Sec. V. Several computational details are provided in the Appendices.

II. MODEL AND METHODS

The spin-half bilayer Heisenberg model on the square lattice is described by the Hamiltonian

$$H = J' \sum_i \mathbf{S}_{i1} \cdot \mathbf{S}_{i2} + J \sum_{\langle i,j \rangle} (\mathbf{S}_{i1} \cdot \mathbf{S}_{j1} + \mathbf{S}_{i2} \cdot \mathbf{S}_{j2}), \quad (1)$$

where spins $\mathbf{S}_{i\mu}$ reside on the lower ($\mu = 1$) and upper ($\mu = 2$) layer within the ith unit cell of a square lattice, where the lattice constant is set to $a = 1$ in the following, as is the interlayer distance $d = 1$. It should, however, be noted that our results do not depend on the value of a and d, as different choices of these lattice parameters affect only the absolute scale of the momentum space vectors. Note also that each unit cell contains an interlayer (rung) bond of the bilayer lattice. Here, J (J') denote the intralayer (interlayer) exchange coupling. The model exhibits, in addition to the internal SU(2) spin symmetry and the square-lattice space-group symmetry, also a layer inversion symmetry in the layer indices (1 and 2). We account for this additional quantum number when assigning a third component to an originally two-dimensional momentum space vector, such that $\mathbf{k} = (k_x,k_y,k_z)^\intercal$, with $k_z = 0$ or π, denoting the symmetric and antisymmetric channel with respect to layer inversion, respectively. Correspondingly, in position space, each spin is also assigned a transverse position, with respect to its layer index, such that $\mathbf{r}_{i\mu}$ is a three-component position vector, with the third component equal to 0 (1), for $\mu = 1$ ($\mu = 2$), respectively.

Of particular interest for our analysis is the dynamical spin structure factor, which is defined with respect to the Heisenberg-picture time evolution of the spin operators as (with N_s denoting the number of spins)

$$S_S(\omega,\mathbf{k}) = \frac{1}{N_s} \int dt \sum_{i,j,\mu,\nu} e^{i(\omega t - \mathbf{k}\cdot(\mathbf{r}_{i\mu} - \mathbf{r}_{j\nu}))} \langle \mathbf{S}_{i\mu}(t) \cdot \mathbf{S}_{j\nu}(0) \rangle. \quad (2)$$

We will also refer to the $k_z = 0$ ($k_z = \pi$) cases as the symmetric or even (antisymmetric or odd) sector. In the presence of long-range antiferromagnetic order, one may furthermore distinguish the components of $S_S(\omega,\mathbf{k})$ parallel and transverse with respect to the order parameter direction, in which case $S_S(\omega,\mathbf{k})$ represents a rotational average probed by the quantum Monte Carlo simulations.

For completeness, we finally note how the symmetric and antisymmetric structure factors, introduced above for an isolated bilayer, relate to the neutron scattering intensity for a three-dimensional system composed out of parallel stacked bilayers. For a lattice constant a within each of the square lattice layers and an interlayer distance d, the scattering intensity for a scattering wave vector $\mathbf{q} = (q_x,q_y,q_z)^\intercal$ is then proportional to the structure factor

$$S_S^{\text{stack}}(\omega,\mathbf{q}) = \cos^2(d\,q_z/2)\, S_S(\omega,a\,q_x,a\,q_y,0) + \sin^2(d\,q_z/2)\, S_S(\omega,a\,q_x,a\,q_y,\pi), \quad (3)$$

see, e.g., the discussions in Refs. [30,31].

In addition to the spin-spin correlations, we also consider in the following interlayer singlet bond (or spin-exchange) terms:

$$B_i = \mathbf{S}_{i1} \cdot \mathbf{S}_{i2}, \quad (4)$$

which define a corresponding scalar response function in terms of the dynamical structure factor (with N denoting the number of interlayer bonds, and $N_s = 2N$)

$$S_B(\omega,\mathbf{k}) = \frac{1}{N} \int dt \sum_{i,j} e^{i(\omega t - \mathbf{k}\cdot(\mathbf{r}_i - \mathbf{r}_j))} \langle B_i(t) B_j(0) \rangle, \quad (5)$$

where here $\mathbf{k}$ and the $\mathbf{r}_i$ denote two-dimensional square lattice k space and lattice position vectors (i.e., with a vanishing third component), since the singlet operators B_i reside at positions $\mathbf{r}_i$ on the square lattice spanned by the interplanar (J') rung bonds. Given its scalar nature, we refer to $S_B(\omega,\mathbf{k})$ also as the dynamical singlet structure factor.

After having introduced the model and the relevant observables for our study, we next give here an overview of the various methods that we used. Details on the calculations with these methods can be found in the various appendices, as indicated below.

A. Quantum Monte Carlo approach

For the quantum Monte Carlo calculations, we used the stochastic series expansion method with directed loop updates [32–34]. In the simulations, we considered finite systems with $N_s = 2L^2$ lattice sites and periodic boundary conditions in both square lattice directions $\mathbf{x} = (1,0)^\intercal$, and $\mathbf{y} = (0,1)^\intercal$. In order to access ground-state properties, the inverse temperature β must be chosen sufficiently large. This typically requires $\beta J \geqslant 2L$. In our simulations, we considered mainly finite systems with $L = 20$ with $N_s = 800$ sites at $\beta J = 50$, unless specified otherwise.

To access the dynamical spin structure factor using the quantum Monte Carlo simulations, we efficiently [35] measure the imaginary-time displaced spin-spin correlation functions directly in Matsubara frequency representation, which is related to $S_S(\omega,\mathbf{k})$ via

$$S_S(i\omega_n,\mathbf{k}) = \int_0^\infty d\omega\, \frac{\omega}{\pi} \frac{(1-e^{-\beta\omega})}{\omega^2+\omega_n^2}\, S_S(\omega,\mathbf{k}). \qquad (6)$$

Here, $\omega_n = 2\pi n/\beta$ for $n = 0,1,2,\ldots$ are bosonic Matsubara frequencies. One typically needs values of n up to 160 to access the leading $1/\omega_n^2$ asymptotic behavior of $S_S(i\omega_n,\mathbf{k})$. The numerical inversion of Eq. (6) to obtain $S_S(\omega,\mathbf{k})$ from the Matsubara frequency quantum Monte Carlo data $S_S(i\omega_n,\mathbf{k})$ was performed using the stochastic analytic continuation method in the formulation of Ref. [36]. While such numerical analytic continuation methods tend to broaden inherent spectral features, they can still resolve a low number of excitation poles also from a separate continuum spectral contribution, depending on the quality of the imaginary-time data.

In order to efficiently access the dynamical singlet structure factor $S_B(\omega,\mathbf{k})$ of the bond-bond correlations from the quantum Monte Carlo simulations, we measured the corresponding bond-bond correlation functions in imaginary time, binned over finite-width imaginary-time windows [35]. Using an appropriate kernel for the analytic continuation, we then relate $S_B(\omega,\mathbf{k})$ directly to this imaginary-time binned quantum Monte Carlo data, without the need for an intermediate unfolding of the bin-resolution correlation function. Further details of this measurement setup are provided in Appendix A.

B. Spin-wave theory

Upon expressing the spin fluctuations about the classical magnetically ordered state using the standard Holstein-Primakoff representation [37], one arrives in the harmonic approximation at the linear spin-wave description of the magnetic excitations in the ordered phase. As discussed in Sec. III, the comparison between the spin-wave results and the dynamical structure factor as obtained from the quantum Monte Carlo simulation improves upon taking into account corrections beyond the harmonic approximation in the spin-wave expansion. This has been done here by considering the next-to-leading order in the $1/S$ expansion of the Hamiltonian, and by performing a mean-field decoupling of the bosonic interaction terms to renormalize the coupling constants. Details on both the linear and higher-order spin-wave theory calculations are presented in Appendix B.

C. Perturbation theory in $1/g$

In the quantum-paramagnetic phase, an efficient description of the spin dynamics can be obtained from perturbation theory in the intralayer coupling J, i.e., starting from the limit of decoupled dimers which form a product state of singlets in the limit $J = 0$. Exciting a single rung gives rise to a triplet excitation, which can delocalize for finite J, giving rise to a gapped excitation mode. We perform a systematic expansion for the dynamical spin structure factor in $1/g$ up to second order for the triplet dispersion and to linear order in the spectral weight. While for the antisymmetric channel closed explicit expressions are obtained, we need to perform a numerical diagonalization of the effective interaction Hamiltonian in the two-triplon sector to access the symmetric channel of the dynamical spin structure factor. Details on these calculations are provided in Appendix C.

D. Bond-operator-based $1/d$ expansion

Bond operators [38] were initially introduced to efficiently describe the paramagnetic phase of spin-half coupled-dimer magnets, the square lattice bilayer considered here being a prominent example. In this approach, one introduces bosonic operators corresponding to spin-1 excitations (often called *triplons* [26]) atop a singlet background [39,40]. Generalizations of the bond-operator approach to magnetically ordered states [22] and to arbitrary spin [41] have been investigated in the past. Moreover, it was recently shown [42,43] that bond operators enable a controlled description of coupled-dimer systems across the entire phase diagram using $1/d$ as a small parameter, where d is the spatial dimension: relevant observables can be obtained in a systematic $1/d$ expansion once the dimer lattice has been generalized to d space dimensions (for details we refer to Refs. [42,43]). In particular, the dispersion relation of triplon excitations in the disordered phase as well as that of gapless transverse modes and the gapped longitudinal mode in the ordered phase were reported along with their corresponding spectral weights in the dynamic spin susceptibility. As will be discussed in Sec. III, a comparison with the dispersions obtained from quantum Monte Carlo shows very good agreement after a proper mapping of the model parameters (the coupling ratio g), as explained in Sec. III. In order to study the amplitude (Higgs) mode, we also calculated the bond-bond correlation to leading order in $1/d$. A comparison with quantum Monte Carlo results will be discussed in Sec. IV. We find that to leading order in $1/d$, the longitudinal mode gives rise to a single mode spectral

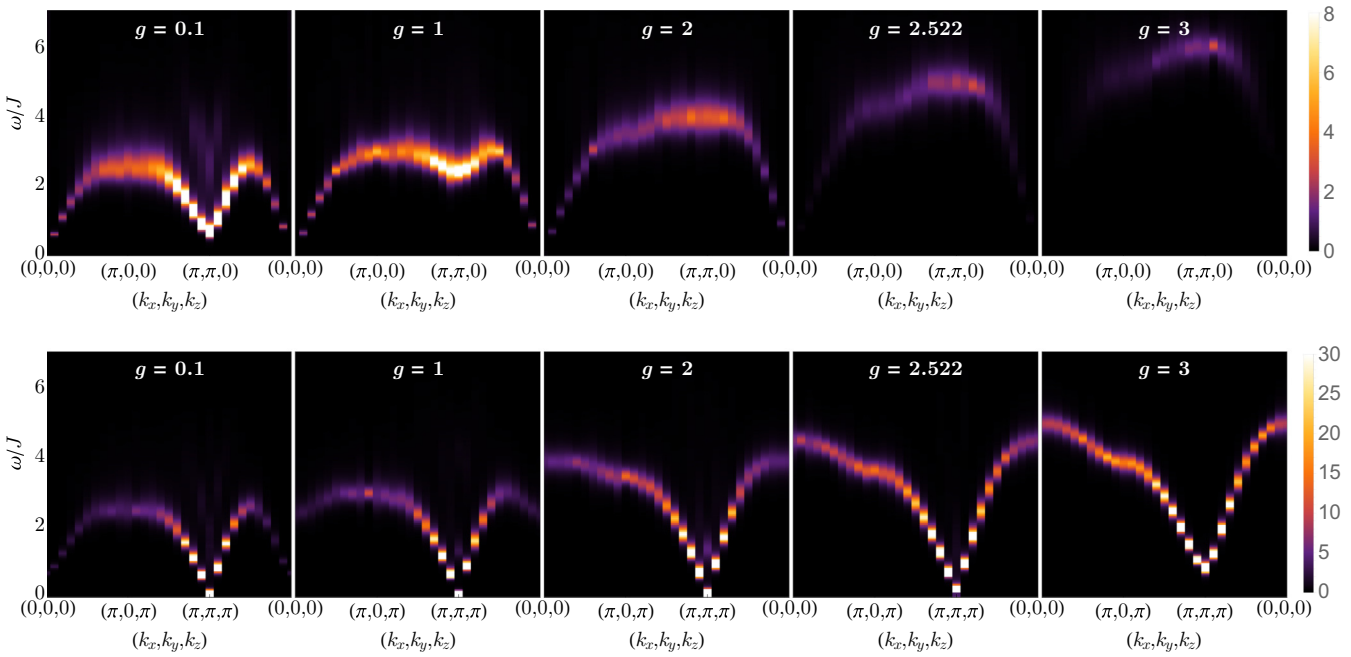

FIG. 1. (Color online) Dynamical spin structure factor $S_S(\omega,\mathbf{k})$ in the symmetric (top) and antisymmetric (bottom) channel for the spin-half Heisenberg model on the square lattice bilayer at different ratios $g = J'/J$ of the interlayer (J') to intralayer (J) coupling strength along the indicated path in the two-dimensional Brillouin zone.

contribution to the inter-layer singlet dynamical structure factor. Further details on the bond-operator calculations can be found in Appendix D.

III. DYNAMICAL SPIN STRUCTURE FACTOR

The dynamical spin structure factor $S_S(\omega,\mathbf{k})$ is directly related to the scattering intensity as probed by inelastic neutron scattering experiments. Here, we monitor the evolution of $S_S(\omega,\mathbf{k})$ upon varying the interaction ratio g across the quantum critical point.

A. Quantum Monte Carlo results

We first present the results from the quantum Monte Carlo simulations for the dynamical spin structure factor. In Fig. 1, the dynamical spin structure factor $S_S(\omega,\mathbf{k})$ is shown for different values of g, each along a standard-path in the two-dimensional Brillouin zone, for the symmetric ($k_z = 0$) and the antisymmetric ($k_z = \pi$) channel, separately. The structure factor in the antisymmetric channel is dominated by a sharp single-mode-like contribution that softens in the antiferromagnetic regime at $\mathbf{k} = \mathbf{Q}$, the magnetic Bragg peak position $\mathbf{Q} = (\pi,\pi,\pi)^\intercal$, while it exhibits a fully gapped branch in the quantum disordered regime, with a minimum gap $\Delta_T(g)$ in the dispersion, located at $\mathbf{k} = \mathbf{Q}$. In the antiferromagnetic region, the dispersive feature traces the dispersion relation of the antiferromagnetic magnon (Goldstone) excitation mode, while in the quantum disordered region, it follows the gapped triplon dispersion. Both these relations will be substantiated by a direct comparison to spin-wave theory and perturbation theory calculations in $1/g$ for the antiferromagnetically ordered and quantum disordered regime respectively, as discussed below in Sec. III B.

Approaching the quantum critical point, we observe enhanced finite-size effects due to the algebraic growth of the correlation length within the quantum critical region. We anticipate the most pronounced finite-size corrections to appear right at the quantum critical point: based on the relativistic invariance with a dynamical critical exponent $z = 1$, at low energies, finite-size corrections of the peak position proportional to $1/L$ dominate at criticality. Indeed, enhanced finite-size corrections at the quantum critical point were reported recently for the low-energy dispersion of the Goldstone mode [44], and are visible in Fig. 1 for $g = 2.522$, where a small finite-size gap at $\mathbf{k} = \mathbf{Q}$ can be clearly resolved. A finite-size study of the dynamical spin structure factor, shown in Fig. 2, indeed reveals a linearly vanishing finite-size excitation gap as a function of $1/L$, as shown in the inset of that figure.

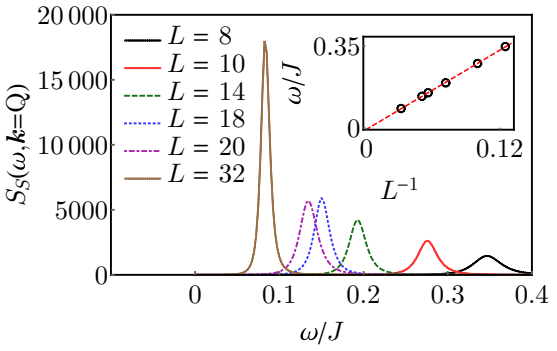

FIG. 2. (Color online) Dynamical spin structure factors $S_S(\omega,\mathbf{k} = \mathbf{Q})$ for the spin-half Heisenberg model on the square lattice bilayer at the quantum critical point, $g = g_c$. The finite-size scaling of the excitation gap is shown vs $1/L$ in the inset.

The symmetric channel exhibits in the antiferromagnetically ordered phase a similarly sharply resolved distribution of the spectral weight, which however softens near the $\Gamma = (0,0,0)^\intercal$ point. Its dispersion follows to a very good accuracy that of the antisymmetric mode with a shift of the in-plane momentum by (π,π). At the Γ point, the spectral weight is completely suppressed for all values of g: this relates to the fact that spin fluctuations at the Γ point, i.e., in the uniform magnetization, vanish, due to the SU(2) symmetry of H. The gap at $\mathbf{k} = (\pi,\pi,0)^\intercal$ decreases upon approaching the limit of decoupled layers ($g \to 0$), and in the limit of decoupled layers, the structure factor in the symmetric channel softens at $\mathbf{k} = (\pi,\pi,0)^\intercal$, which is the single-layer Bragg peak position (note that at exactly $g = 0$ the signal vanishes completely in the antisymmetric channels, since for $J' = 0$ the spins decouple between the layers, while any weak, finite $g > 0$ leads to a locking of the antiferromagnetic order between the layers). By contrast to the antisymmetric channel, the overall spectral weight in the symmetric channel is strongly suppressed for large values of g: well in the quantum disordered regime, only a faint spectral weight distribution is present in the symmetric channel, while the antisymmetric channel provides a direct trace of the dispersion relation of the gapped triplon excitation mode.

In addition to the sharp, single-mode features that we mainly discussed thus far, the structure factor in the ordered phase also exhibits a broader distribution of spectral weight for energies above the single-mode threshold due to the multimagnon continuum. This is seen more explicitly from the data for $(k_x,k_y) = (\pi,0)$ and $(\pi/2,\pi/2)$ in both the symmetric and the antisymmetric channel in Fig. 3, shown with a logarithmic scale on the vertical axis. On general grounds, it proves difficult to extract an accurate shape of the continuum contribution to the structure factor from an analytic continuation, in particular given the additional presence of a sharp magnon peak. For this reason we first concentrate here in Fig. 3 on momenta away from the magnetic ordering wave vector $\mathbf{Q}$; the continuum contribution at $\mathbf{k} = \mathbf{Q}$ will then be discussed in more detail in Sec. IV, since it is of particular interest with regards to the possibility of observing a Higgs peak in the spin structure factor.

We can draw several general observations and perform a comparison to previous work based on the data shown in Fig. 3: for low, finite values of g (cf. the case of $g = 0.1$ in the left-most panel of Fig. 3), the data for the symmetric and the antisymmetric channel are very similar, and for both momenta essentially relate to the response of a single square lattice layer. The single-layer case was previously carefully analyzed by quantum Monte Carlo methods in Ref. [46], using, however, a different analytic continuation approach that relied on an explicit ansatz for the spectral function in terms of a sharp magnon peak plus a parametrized form of the mutimagnon continuum. In addition, the authors of Ref. [46] performed a separate calculation of the structure factor contributions from the transverse and the longitudinal sector by applying a weak, fine-tuned staggered magnetic field to the finite-size systems, in order to induce in an explicit form the SU(2) symmetry breaking on finite systems which emerges in the original model only in the thermodynamic limit. Even given these different approaches, our data for low g are in qualitative agreement with several main conclusions of Ref. [46]; in particular, the continuum contribution to the overall spectral weight is more extended at $(\pi,0)$, and the magnon peak resides at slightly larger energies at $(\pi/2,\pi/2)$ as compared to the other momentum. In Ref. [46], these observations are discussed in connection to limitations of spin-wave theory to accurately describe the magnetic excitations of the square lattice Heisenberg model as well as related experimental findings. We comment further on the comparison of our results to spin-wave theory in Sec. III B.

From Fig. 3, we furthermore observe that at larger values of g, differences between the symmetric and the antisymmetic channel become pronounced for both momenta considered here. In particular, the peak-heights in the symmetric channel are reduced, reflecting the loss of spectral weight of the structure factor in the symmetric channel inside the quantum disordered regime that we already mentioned above, while for the antiferromagnetic channel, we observe a sharpening of the magnon peaks upon increasing g.

We also note that the structure factor for the quantum critical system at $g = g_c$ still exhibits a rather sharp overall shape, as can be seen in Figs. 2 and 3. Beyond the general difficulty in quantifying the width of spectral data obtained via an analytic continuation, we relate this observation also to the fact that the anomalous critical exponent η is very small for the quantum critical point under consideration here. Indeed, this quantum critical point belongs to the three-dimensional O(3) universality class, with $\eta \approx 0.03$ [45]. This confers to the critical continuum the appearance of a relatively sharp peak.

The bilayer Heisenberg model is obtained as the effective low-energy theory for the spin dynamics within the

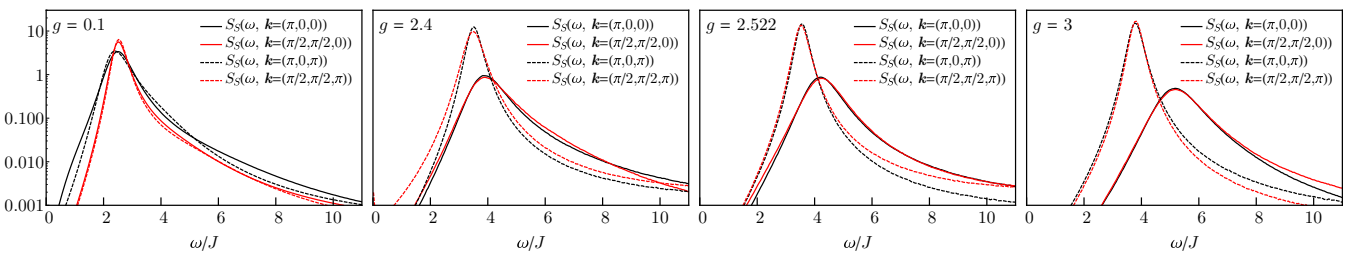

FIG. 3. (Color online) Dynamical spin structure factor $S_S(\omega,\mathbf{k})$ for the spin-half Heisenberg model on the square lattice bilayer for different values of g at momenta $(\pi,0)$ and $(\pi/2,\pi/2)$ in both the symmetric (full lines) and the antisymmetric channel (dashed lines). A logarithmic scale is used on the vertical axes.

Mott insulator, in the strong-coupling limit of the half-filled Hubbard model on the square lattice bilayer. At strong local Hubbard repulsion $U \gg t$, we thus expect that the evolution of the spectral weight in the dynamical spin structure factor, as described above, can be observed also in the Hubbard model, upon tuning the ratio t'/t of the interlayer tunneling (t') to the intralayer tunneling (t). It is less clear, however, that this also holds in the intermediate coupling regime, where U is of order the bandwidth, and where residual charge fluctuations allow for higher-order spin exchange processes. To address this question, we performed also determinantal quantum Monte Carlo simulations for the Hubbard model on the square lattice bilayer. From our simulations, we find that also in the intermediate coupling region the dynamical spin structure factor exhibits the characteristic behavior that we observed in the Heisenberg limit. We provide details on these results for the Hubbard model in Appendix E. Returning here to the Heisenberg model, we next perform a detailed comparison of the quantum Monte Carlo results to the various theoretical approaches that we listed in Sec. II.

B. Comparison to analytic results

In the following, we compare our quantum Monte Carlo data to the results obtained within (i) linear and higher order spin-wave theory, (ii) the $1/g$ perturbation theory as well as (iii) the $1/d$ expansion within the bond-operator approach. While the spin-wave and the large-g approach are restricted to the ordered and quantum disordered regimes, respectively, the $1/d$ expansion allows us to calculate appropriate structure factors throughout the whole phase diagram. The upper two rows of Fig. 4 and the upper row of Fig. 5 show the dispersion relations for the region below and above the quantum critical point, respectively. In these panels, the mode dispersions from the quantum Monte Carlo data have been obtained by the peak positions in the spectral weight distribution, with the symbol size indicating the estimated uncertainty. In addition to comparing the dispersions, we also compare, in the lower rows of Figs. 4 and 5, the integrated spectral weight

$$S_S(\mathbf{k}) = \int d\omega\, S_S(\omega,\mathbf{k}), \tag{7}$$

which in the quantum Monte Carlo simulations is conveniently obtained from the equal-time spin-spin correlations, to the results from spin-wave theory and the $1/g$ perturbation theory as well as the bond-operator theory. For the ordered phase, we performed the bond-operator theory calculations for the integrated spectral weight only in the harmonic approximation, while for the disordered phase, we also considered the leading $1/d$ corrections. We also note that, in contrast to the mode dispersion, the integrated spectral weight can be obtained directly from the quantum Monte Carlo simulations without the need of performing the analytic continuation.

We first compare our numerical results to the dispersions obtained from spin-wave theory. From the upper two panels of Fig. 4, we find that (i) linear spin-wave theory, while providing a good overall account of the spin-wave dispersion, systematically underestimates the spin-wave energies, and (ii) the higher order spin-wave theory approximation provides a significant improvement to the overall dispersions. As

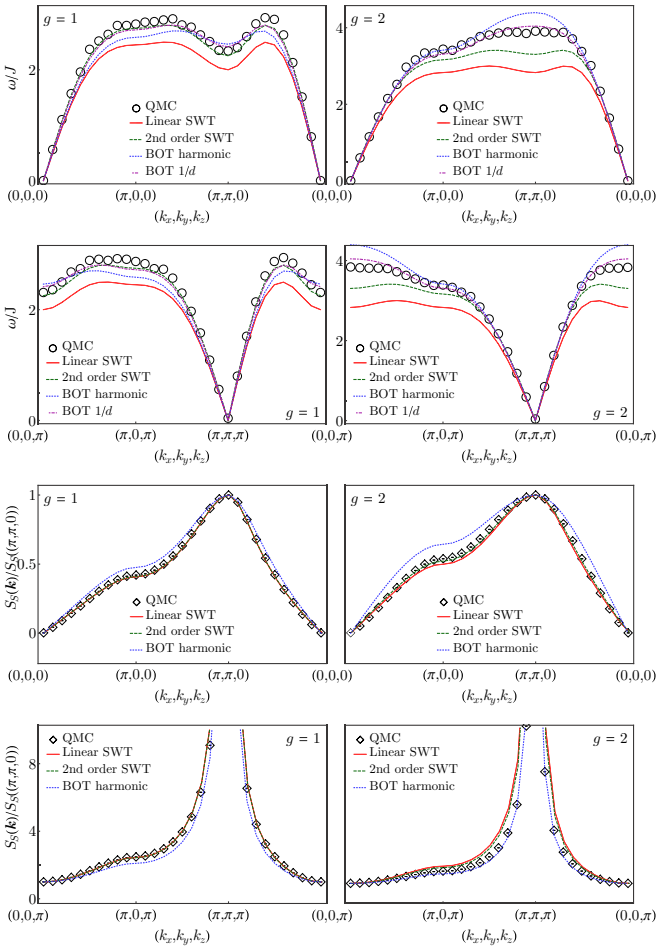

FIG. 4. (Color online) Comparison of the dynamical spin structure factor at different ratios $g = J'/J$ inside the antiferromagnetically ordered region for the spin-half Heisenberg model on the square lattice bilayer between the quantum Monte Carlo (QMC) results and linear and second-order spin-wave theory (SWT) as well as bond-operator theory (BOT), both in harmonic approximation and including leading $1/d$ corrections. The upper panel compares the dispersion of the single-mode contribution, and the lower panel the integrated spectral weight $S_S(\mathbf{k})$. Here, the results for the symmetric (antisymmetric) channel have been normalised by the value of $S_S((\pi,\pi,0))$ ($S_S(0)$), corresponding to the maximum (minimum) value in that channel.

detailed in Appendix B, the net effect of the second order corrections to linear spin-wave theory can be expressed in terms of a g-dependent renormalization of the coupling ratio g, which for $g > 1$ leads to an enhanced effective coupling ratio $g_{\text{eff}} > g$, which results in the hardening of the spin-wave dispersion, as observed in Fig. 4. As discussed in Appendix B, we find that an even further, heuristic renormalization of g_{eff} allows us to obtain even better matches of the effective spin-wave theory dispersion to the numerical results.

With respect to the integrated spectral weight $S_S(\mathbf{k})$, which is shown in the lower two panels of Fig. 4, we find that up to intermediate coupling ratios (cf. the case $g = 1$ in the left panels of Fig. 4), both linear and second order spin-wave theory provide a good overall account of the spectral weight distribution in the symmetric channel. Upon closer inspection,

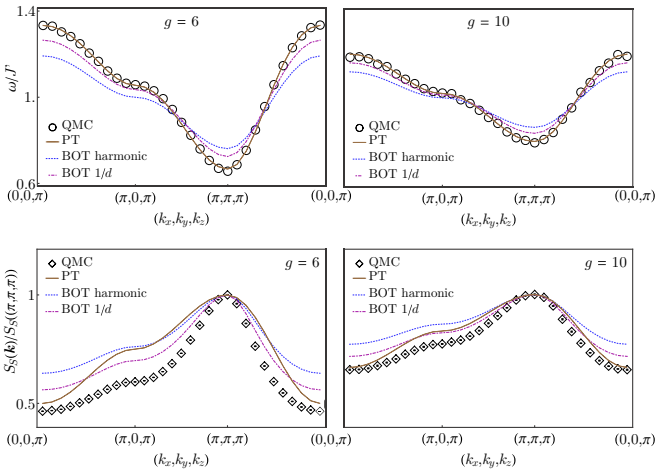

FIG. 5. (Color online) Comparison of the dynamical spin structure factor in the antisymmetric channel at different ratios $g = J'/J$ well inside the quantum disordered region for the spin-half Heisenberg model on the square lattice bilayer between the quantum Monte Carlo (QMC) results and $1/g$ perturbation theory (PT) as well as bond-operator theory (BOT) in both harmonic approximation and with leading $1/d$ corrections included. The upper panel compares the dispersion of the single triplon contribution, and the lower panel the integrated spectral weight $S_S(\mathbf{k})$.

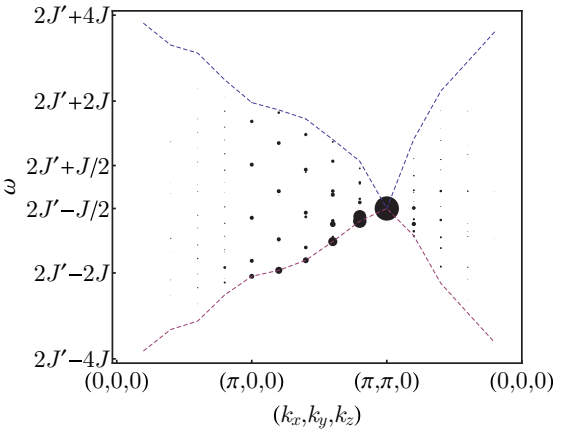

FIG. 6. (Color online) Distribution of the amplitude in the dynamical spin structure factor $S_S(\omega,\mathbf{k})$ for the symmetric sector ($k_z = 0$) as obtained within the $1/g$ perturbation theory for the numerical diagonalisation of the effective Hamiltonian within the two-triplon sector on a $L = 10$ system. The sizes of circles are proportional to the amplitude at the center positions. Dashed lines indicate the upper and lower bounds of the continuum.

however, one notices that the spin-wave theory results for $g = 1$ fall slightly below the quantum Monte Carlo data for $S_S(\mathbf{k})$ for $\mathbf{k}$ near $(\pi,0,0)^\intercal$. This difference gets more pronounced upon increasing g towards the quantum critical point, cf. the data for $g = 2$ in the right panels of Fig. 4. The failure of low-order spin-wave theory to fully account for the spectral properties for wave vectors near $\mathbf{k} = (\pi,0)^\intercal$ has been noticed previously for the case of a single-layer Heisenberg model (i.e., $g = 0$; cf., e.g., Ref. [46] for an extended discussion) and was recently linked to strong attractive magnon-magnon interactions that induce a Higgs resonance from two-magnon states [47]. One would then expect that the increase in the deviation to low-order spin-wave theory that we observe in the integrated spectral weight for $g = 2$ relates to an enhancement in the Higgs resonance formation. If fact, as discussed in Sec. III, we can identify a well defined low-energy Higgs peak in the singlet structure factor for g near g_c, which adds further support to this scenario.

For the antisymmetric mode, we find that both linear and higher-order spin-wave theory accounts well for the integrated spectral weight distribution for $g = 1$, while they overestimate the integrated spectral weight near the ordering wave vector, $\mathbf{k} = \mathbf{Q}$, closer to g_c, cf. the data for $g = 2$ in Fig. 4, reflecting the fact that quantum fluctuations of the order parameter, are underestimated within these approximations.

Next, we focus on the quantum disordered region, and discuss the comparison to the $1/g$ perturbation theory. Well inside the quantum disordered region, we find that the $1/g$ perturbation theory, presented in Appendix C, provides a rather good account of the quantum Monte Carlo data. A corresponding comparison of the triplon dispersion and the corresponding spectral weight (i.e., in the antisymmetric channel) for $g = 6$ and 10 is shown in Fig. 5. While the triplon dispersion is obtained very accurately within our $1/g$ perturbation calculations for both values of g, the integrated spectral weight at $g = 6$ already exhibits somewhat larger quantitative differences than at $g = 10$. As detailed in Appendix C, we performed the perturbative calculations for the triplon dispersion up to quadratic order in $1/g$, while the spectral weight was obtained up to linear order, and thus is expected to be less accurate at larger values of $1/g$. Nevertheless, the overall shape of the spectral weight distribution is well represented at this leading order already.

Thus far, in discussing the quantum disordered region, we considered only the antisymmetric channel, which is dominated by the gapped triplon mode with a pronounced spectral weight. However, within $1/g$ perturbation theory, we can also obtain a quantitative description of the faint spectral weight distribution for the symmetric channel in the quantum disordered regime. Figure 6 shows the result for the dynamical spin structure factor in the symmetric channel as obtained from the $1/g$ perturbation expansion by a numerical diagonalization of the effective Hamiltonian within the two-triplon sector for a $L = 10$ system. The structure factor is seen to display a concentration of the spectral weight at $\mathbf{k} = (\pi,\pi,0)^\intercal$, which corresponds to an eigenstate of the effective Hamiltonian in that sector. This is in good agreement with the quantum Monte Carlo data that also exhibit a concentration of the spectral weight for the symmetric channel near $\mathbf{k} = (\pi,\pi,0)^\intercal$, cf., e.g., the data for $g = 3$ in Fig. 1. One furthermore finds from the perturbative calculations, that the amplitude of the symmetric channel is of order $(1/g)^2$, and thus vanishes in the limit $J/J' \to 0$ (cf. Appendix C for details of the calculation), which is reflected also by the quantum Monte Carlo data.

The comparison of the quantum Monte Carlo data to the bond operator-based $1/d$ expansion requires an appropriate mapping from the coupling ratio g to the parameter q (defined as $q = Jd/J' = d/g$, with d the dimension of the system, here, $d = 2$) that enters the $1/d$ expansion. Indeed, within the

$1/d$ expansion, the quantum critical point is obtained as $q_c = 1/2 + 3/(16d) + \mathcal{O}(1/d^2)$, so that at the harmonic level (i.e., without $1/d$ corrections) $q_c = 1/2$, while including first-order corrections in $1/d$ leads to $q_c = 0.59375$, to be compared to the value of $(q_{\rm QMC})_c = d/g_c = 0.7930(2)$ that results from the (accurate) quantum Monte Carlo estimate of g_c. We need to account for this difference when performing the comparison, in particular in the vicinity of g_c. For a given value of $g \leqslant g_c$, we fix the value of q such that $(q - q_c)$ equals the corresponding absolute distance in $q_{\rm QMC} = d/g$ to $(q_{\rm QMC})_c$, i.e., such that

$$q - q_c = q_{\rm QMC} - (q_{\rm QMC})_c. \tag{8}$$

In the quantum disordered phase, $g > g_c$, it is more appropriate to relate the parameters by considering a fixed *relative* distance to the quantum critical point, i.e., a value of q is obtained, such that

$$\frac{q - q_c}{q_c} = \frac{q_{\rm QMC} - (q_{\rm QMC})_c}{(q_{\rm QMC})_c}. \tag{9}$$

The corresponding mode dispersions are shown in the upper panels of Fig. 4 for $g < g_c$ and Fig. 5 for $g > g_c$, respectively, while the lower panels of these figures show the comparison in the integrated spectral weight $S_S(\mathbf{k})$. We find that with the above parameter mappings, the bond-operator theory provides a good qualitative account of both the spin-wave dispersion and the triplon dispersion within this unified approach, at least when the leading $1/d$ corrections beyond the harmonic approximation are taken into account. Nevertheless, the harmonic approximation already keeps track of the leading dispersive features and provides a good account of the integrated spectral weight in both phases. For the following discussion of the amplitude mode, we thus limited the bond-operator theory calculations to the harmonic level.

IV. AMPLITUDE (HIGGS) MODE

The longitudinal, amplitude fluctuations of the order parameter field need to be properly taken into consideration in a quantitative description of the quantum critical bilayer Heisenberg antiferromagnet and its low energy properties [21,22]. For example, within bond-operator theory calculations, the amplitude mode is found to soften upon approaching the quantum critical point, thus restoring the SU(2) symmetry, while it hardens towards an elevated energy scale of order $4J$ in the limit of decoupled layers ($J' = 0$), rendering it insignificant with respect to the order-parameter fluctuations well inside the ordered phase [21,22]. While the relevance of the amplitude mode on, e.g., the order parameter strength and the critical value of g has been well studied in the past, only recently have possible direct signatures of the amplitude mode and appropriate experimental probes been addressed. In particular, it has been argued that response functions which couple to the square of the order parameter will show a distinct peak from the amplitude mode (Higgs peak), well separated from the multimagnon contribution to the overall spectral weight in the ordered phase, close to the quantum critical point [5,13].

A. Quantum Monte Carlo results

To quantify these considerations for the bilayer Heisenberg model, we examine in this section the interlayer-bond spin-exchange correlations, in terms of the corresponding dynamical singlet structure factor $S_B(\omega,\mathbf{k})$ introduced in Sec. II. Based on its scalar nature, we expect the correlations of this observable to exhibit in addition to possible multimagnon contributions also a distinct signal from the amplitude mode, most pronounced in the low-energy regime, and within the vicinity of the quantum critical point. In Fig. 7, we show our numerical data for different values of g, taken on a $L = 20$ system at $\beta J = 50$, representative of ground-state expectation values. We obtain for all values of g a spectral contribution to $S_B(\omega,\mathbf{k})$ at elevated energies $\omega \approx 4J$, which does not exhibit a strong dependence on the coupling ratio g. In addition, however, we observe in the vicinity of the quantum critical point a distinct feature in the low-energy region, i.e., separated from the higher-energy signal. This additional spectral branch is most pronounced in the vicinity of the Γ point, where also its spectral weight is most clearly visible.

To better exhibit the emergence of the low-energy Higgs peak from the multimagnon contribution, we show in Fig. 8 the dynamical singlet structure factor $S_B(\omega,\mathbf{k} = 0)$ at the Γ point for different values of the coupling ratio g_c. Within the range $2 \lesssim g \lesssim g_c$, we detect a separate, low-energy peak split-off from the broad second peak in the spectral weight at elevated energies. The position of the low-energy peak tends towards

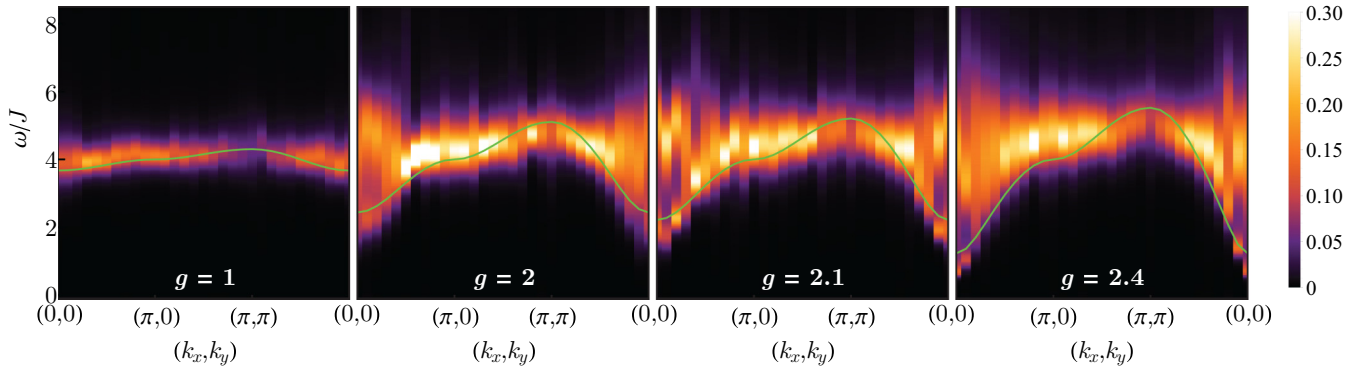

FIG. 7. (Color online) Dynamical singlet structure factor $S_B(\omega,\mathbf{k})$ for the spin-half Heisenberg model on the square lattice bilayer at different ratios $g = J'/J$ of the interlayer (J') to intralayer (J) coupling strength along the indicated path in the two-dimensional Brillouin zone. Also indicated by lines are the amplitude-mode dispersions obtain within the bond-operator theory.

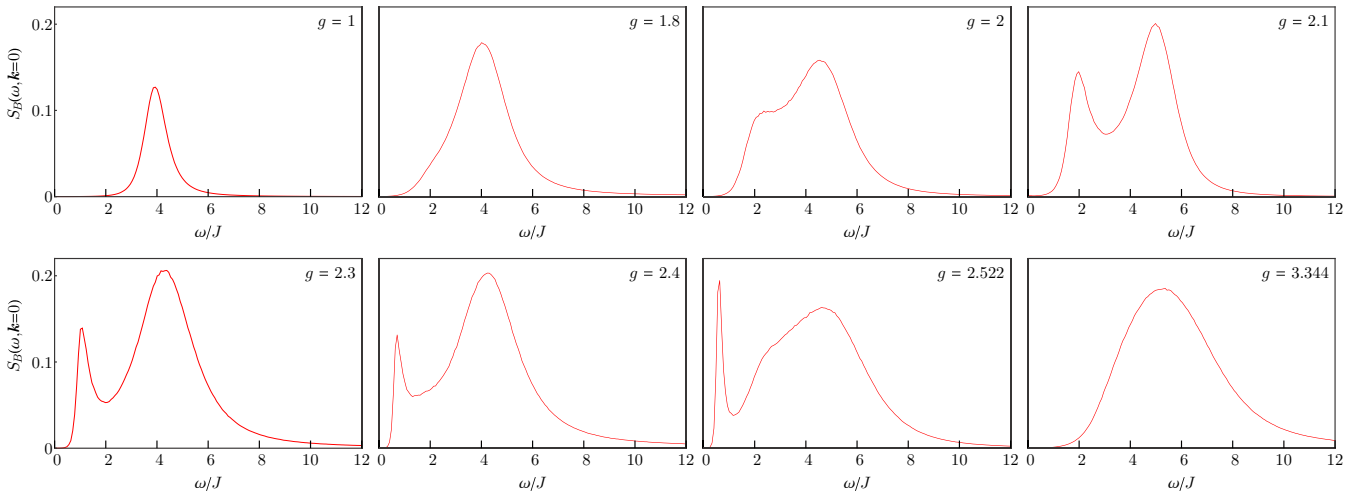

FIG. 8. (Color online) Dynamical singlet structure factor $S_B(\omega,\mathbf{k}=0)$ at the Γ point for the spin-half Heisenberg model on the square lattice bilayer at different ratios $g = J'/J$ of the interlayer (J') to intralayer (J) coupling strength.

lower energies upon tuning g towards its critical value g_c. However, approaching the quantum critical point, we again observe enhanced finite-size effects, most pronounced at the quantum critical point itself. This behavior is illustrated for $g = g_c$ in Fig. 9. We find that for g below about $g \approx 2$, the Higgs peak merges with the second peak, so that a Higgs peak cannot be discerned anymore as a separate spectral feature, restricting its observation to the close vicinity of the quantum critical point.

B. Comparison to bond-operator theory

Within the parameter regime for which we can identify a Higgs-mode peak at the Γ point, we also observe traces of the corresponding mode dispersion near Γ. It is thus interesting to compare our quantum Monte Carlo data to the amplitude-mode dispersion obtained from the bond-operator-based $1/d$ expansion [43]. Referring for details on the $1/d$-expansion calculations of S_B to Appendix D, we compare in Fig. 7 the resulting dispersion relation for the amplitude mode with the quantum Monte Carlo data, using the parameter mapping from Eq. (9).

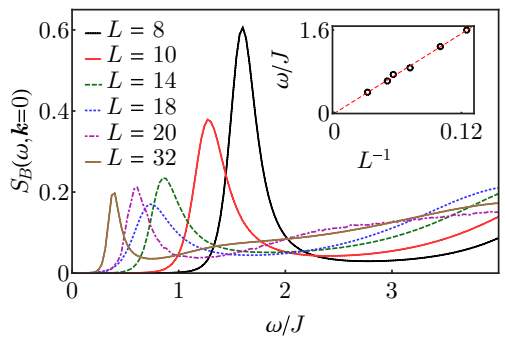

FIG. 9. (Color online) Dynamical singlet structure factor $S_B(\omega,\mathbf{k}=\mathbf{Q})$ for the spin-half Heisenberg model on the square lattice bilayer at the quantum critical point, $g = g_c$. The finite-size scaling of the excitation gap is shown vs $1/L$ in the inset.

Using bond-operator theory we also calculated the spectral weight of the amplitude mode within the harmonic approximation. As discussed in more detail in Appendix D, one finds an enhanced spectral weight in $S_B(\omega,\mathbf{k})$ near the Γ point, in particular, in the vicinity of the quantum critical point, a result which appears to agree with the quantum Monte Carlo data, which also exhibit more pronounced spectral weight for the amplitude mode branch near the Γ point and near the quantum critical point. A more quantitative comparison is limited by the fact that there are contributions (of multimode character) to the spectral weight observed in S_B beyond the pure Higgs-mode contribution considered in Appendix D.

C. Scaling form and comparison to $S_S(\omega,\mathbf{k})$

To analyze further the shape of the Higgs peak, we compare our numerical results to the universal low-energy scaling form of the scalar response function [6] obtained from a $1/N$-expansion of the O(N) model in the quantum critical region,

$$S(\omega) \propto \Delta^{3-2/\nu}\Phi(\omega/\Delta), \tag{10}$$

in terms of the characteristic energy scale in the quantum critical region, $\Delta \propto (1 - g/g_c)^{\nu}$, with the correlation length exponent ν of the three-dimensional O(3) universality class, to which the quantum critical point g_c in the bilayer Heisenberg model belongs. The value of the critical exponent ν has been determined by previous large scale Monte Carlo simulations [48] as $\nu = 0.710(2)$. Finally, Φ denotes a corresponding scaling function. We estimate the g-dependent excitation gap of the amplitude mode $m_H(g)$ (Higgs mass) from the position of the low-energy peak in $S_B(\omega,\mathbf{k}=0)$, and the energy scale $\Delta(g)$ for $g < g_c$ in terms of the triplet excitation gap $\Delta_T(g')$ in the quantum disordered phase, where $g' > g_c$ is the mirrored (with respect to the quantum critical point) coupling ratio defined by $g' - g_c = g_c - g$. In other words, $\Delta(g) = \Delta_T(g_c + (g_c - g))$. For $2 < g < g_c$, i.e., in the region where we can identify a Higgs peak, we find that $m_H(g)/\Delta(g) = 2.6(4)$, in agreement with a previous estimate for this ratio from the effective O(3) field theory [9,12].

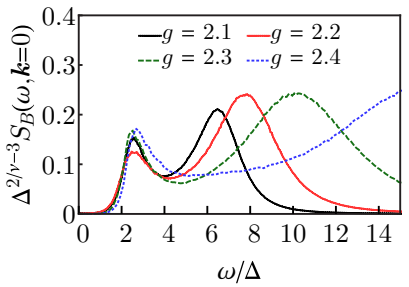

FIG. 10. (Color online) Scaling plot of the dynamical singlet structure factor $S_B(\omega,\mathbf{k}=0)$ at the Γ point for the spin-half Heisenberg model on the square lattice bilayer at different ratios $g = J'/J$ of the interlayer (J') to intralayer (J) coupling strength near the quantum critical pint g_c.

Based on this relation, we show in Fig. 10 the appropriately rescaled data for $S_B(\omega,\mathbf{k}=0)$ from different values of g according to the scaling law in Eq. (10). From this analysis we find that the low-energy part of $S_B(\omega,\mathbf{k}=0)$ relates well to this scaling form, adding further support to the interpretation of the low-energy peak in terms of the amplitude mode. By contrast, the second peak at energies $\omega \approx 4J$ does not follow this scaling form, hence is not part of the universal signal in the response function. In fact, as already mentioned above, we see from Fig. 8 that the position of the second peak does not change much upon varying g, in contrast to the Higgs peak. The observation, that the amplitude mode follows the scalar response function scaling form also implies that in this two-dimensional system, the amplitude mode is only marginally damped in the vicinity of the quantum critical point, i.e., with a width that scales like the Higgs mass m_H near the quantum critical point, thus making the observation of this excitation mode possible.

We find that the quantum Monte Carlo data are consistent also with the low-energy scaling prediction [6] $S(\omega) \propto \omega^3$ in as much as the imaginary-time (τ) data for the bond-bond correlations at $\mathbf{k}=0$ (which are actually calculated in the simulation) agrees with the corresponding decay $S_B(\tau,\mathbf{k}=0) \propto 1/\tau^4$ at large imaginary times (cf. Appendix A for details). However, we cannot independently estimate the large-τ scaling behavior since we are limited by enhanced statistical noise on the imaginary-time data in the relevant τ regime (cf. Appendix A).

In order to contrast further the appearance of the amplitude mode in the dynamical singlet structure factor as compared to the dynamical spin structure factor, we show for different values of g in Fig. 11 both (i) the dynamical singlet structure factor $S_B(\omega,\mathbf{k}=0)$ at the wave vector where S_B softens at g_c, and (ii) the dynamical spin structure factor $S_S(\omega,\mathbf{k}=\mathbf{Q})$ at the Bragg peak position where a possible Higgs mode-contribution would soften at the quantum critical point [43].

As mentioned already in Sec. III A, in the ordered phase, $S_S(\omega,\mathbf{k})$ exhibits in addition to the magnetic Bragg peak an extended tail of spectral weight. This is shown for $\mathbf{k}=\mathbf{Q}$ for several values of g in Fig. 11 (in order to actually exhibit the tail relative to the dominant magnetic Bragg peak signal, we have adopted a logarithmic scale on the vertical axis of this figure). Atop a background signal that falls off with increasing ω, and which is expected from general considerations in the symmetry-broken phase [16], we observe two broad additional features in $S_S(\omega,\mathbf{Q})$ at $\omega \approx J$ and $\omega \approx 4J$, respectively. Compared to the magnetic Bragg peak, both these features are significantly broader and of suppressed spectral weight. These features do not exhibit systematic trends upon varying g, apart from weak shape variations for different values of g. By contrast, the data for $S_B(\omega,\mathbf{k}=0)$ exhibit a clear Higgs peak split-off at $g \approx 2$, that we already analyzed above, with a g-dependent peak position and a shape that agrees with the scalar response function scaling form. Figure 11 illustrates how the presence of the extended residual spectral weight tail beyond the magnetic Bragg peak masks a possible observation of the low-energy Higgs peak in the dynamical spin structure factor even near criticality, in contrast to the scalar response function, which is strongly suppressed at low energies. Furthermore, we find that both structure factors show an enhanced spectral weight in the form of a broad peak at similarly elevated energies $\omega \approx 4J$, suggesting that the spectral weight observed in $S_B(\omega,\mathbf{k})$ in this energy range is dominated by multimagnon contributions.

We finally note that we also examined using the quantum Monte Carlo simulations the intraplanar bond-bond correlations, and find in the symmetric sector (with respect to layer inversion) a similar (but weaker) amplitude-mode contribution emerging in the low-energy region, while no such feature is observed for the antisymmetric channel. As noted in Appendix D, this observation also agrees with the bond-operator-based $1/d$ expansion calculations of the intraplanar bond-bond correlations.

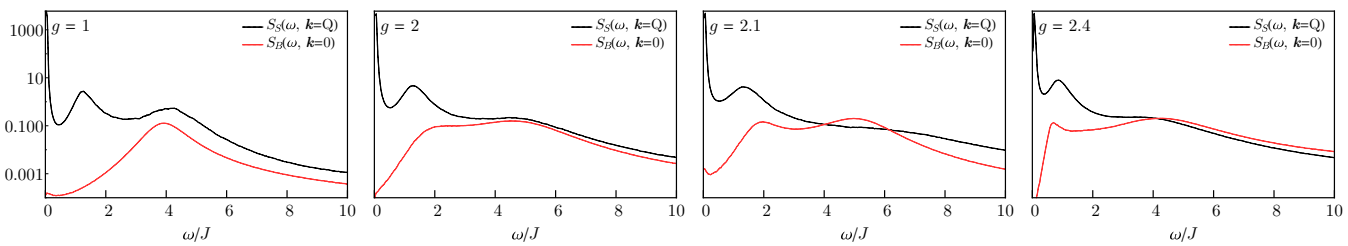

FIG. 11. (Color online) Comparison between the dynamical spin structure factor $S_S(\omega,\mathbf{k}=\mathbf{Q})$ and the dynamical singlet structure factor $S_B(\omega,\mathbf{k}=0)$ for the spin-half Heisenberg model on the square lattice bilayer at different ratios $g = J'/J$ of the interlayer (J') to intralayer (J) coupling strength. In contrast to S_S, we find S_B to exhibit an emerging Higgs peak, following the scalar response function scaling form, near the quantum critical point. A logarithmic scale is used on the vertical axes.

V. CONCLUSIONS

Using quantum Monte Carlo simulations and a variety of analytical approaches, we have obtained precise information on the dynamical response functions of the spin-1/2 Heisenberg model on a bilayer system of square lattices. We have shown that the transition from two gapless spin-wave excitations in the limit of weakly coupled planes to a single gapped triplon excitation in the strong coupling limit occurs via a rapid suppression of the spectral weight of the symmetric spin-wave mode upon increasing the interlayer coupling. The intensity of that mode in the dynamical spin structure factor probed in neutron scattering is already extremely weak at the quantum critical point where the system becomes gapped, and it is the antisymmetric mode that smoothly connects to the triplon mode of the strong coupling limit. We have also looked for traces of the amplitude (Higgs) modes in various dynamical correlation functions. This mode is clearly visible as a distinct spectral feature in the interlayer-bond dynamical singlet structure factor, which opens to the way to its detection with light scattering. However, this mode is not visible in the dynamical spin structure factor, most likely because it is masked by an almost dispersionless continuum of incoherent excitations. While we considered in our numerical study the rotationally averaged dynamical spin structure factor, one may also employ a polarization analysis in actual neutron scattering experiments to separate the longitudinal from the transverse contribution to the total scattering cross section, with a dominant continuum contribution in the longitudinal component. Both these contributions add up to the rotationally averaged signal with a relative weight ratio of 1 : 2, so that from our analysis, we expect that a possible Higgs mode contribution to the longitudinal component will still be difficult to detect even by a polarization analysis. It is our hope that these conclusions will further motivate the experimental investigation of the dynamical response of bilayer systems.

ACKNOWLEDGMENTS

We thank G. Jackeli, G. Khaliullin, A. Läuchli, K. P. Schmidt, V. Schnells, and A. Völl for discussions and acknowledge support by the Deutsche Forschungsgemeinschaft (DFG) under grant Forschergruppe 1807 (FOR 1807) (FFA, ML, SW) and Sonderforschungsbereich 1143 (SFB 1143) (DGJ, MV) and by the Schweizerischer Nationalfonds zur Förderung der Wissenschaftlichen Forschung. Furthermore, we thank the IT Center at RWTH Aachen University and the JSC Jülich for access to computing time through JARA-HPC and on JUROPA. S.W. thanks the KITP Santa Barbara for hospitality during the program "Entanglement in Strongly-Correlated Quantum Matter." This research was supported in part by the National Science Foundation under Grant No. NSF PHY11-25915.

APPENDIX A: BOND OPERATOR MEASUREMENTS IN QUANTUM MONTE CARLO

To efficiently calculate the dynamical singlet structure factor $S_B(\omega,\mathbf{k})$ within the stochastic series expansion (SSE) formulation of quantum Monte Carlo simulations, we extend an approach put forward in Ref. [35]. It is based on the well-known mapping of the discrete SSE configuration space onto a continuous-time world-line formulation [49]. For hermitian conjugate operators A and B that are constructed from Hamiltonian terms, such as the Fourier modes

$$B_{\mathbf{k}} = \frac{1}{\sqrt{N}} \sum_i e^{-i\mathbf{k}\cdot\mathbf{r}_i} B_i \tag{A1}$$

of the spin-exchange terms of the bond-operators B_i introduced in Sec. II, instead of the imaginary-time (τ) correlation function $\langle A(\tau)B\rangle$, we measure an auxiliary correlation function that is defined in terms of a discrete time grid laid over the τ interval $[0,\beta]$, with width $\delta\tau$. Namely, we consider the Monte Carlo estimator

$$C_{AB}(l\,\delta\tau) = \left\langle \frac{1}{\delta\tau^2}\, N_{A\in[(l+1)\delta\tau,l\delta\tau]}\, N_{B\in[\delta\tau,0]} \right\rangle_{\mathrm{MC}}, \tag{A2}$$

where $\langle\cdot\rangle_{\mathrm{MC}}$ denotes the Monte Carlo expectation value, and $N_{A\in I}$ counts the number of operators A in the SSE operator sequence which lie within the time imaginary-time interval I, while $l = 1,\ldots,L_\tau - 1$, with L_τ given by the number of time-slices, $\beta = L_\tau\,\delta\tau$. Using the periodicity of the SSE configuration, one can further improve the above estimator to

$$C_{AB}(l\,\delta\tau) = \frac{1}{\beta\delta\tau}\langle N_{(A,B),l}\rangle_{\mathrm{MC}}, \tag{A3}$$

where $N_{(A,B),l}$ counts the number of pairs (A,B) in the operator string where A acts l time intervals later than B. This auxiliary correlation function is related to the correlation function $\langle A(\tau)B\rangle$ through a convolution,

$$C_{AB}(l\,\delta\tau) = \int_{-\delta\tau}^{\delta\tau} d\tau\, \frac{\delta\tau - |\tau|}{\delta\tau^2}\langle A(l\,\delta\tau+\tau)B\rangle. \tag{A4}$$

Instead of performing an approximate de-convolution of this relation [35], here we make use of the convoluted kernel

$$K_{\delta\tau}(\omega,\tau) = \int_{-\delta\tau}^{\delta\tau} d\tau'\, \frac{\delta\tau - |\tau'|}{\delta\tau^2}[e^{-(\tau+\tau')\omega} + e^{-(\beta-\tau-\tau')\omega}], \tag{A5}$$

which yields

$$K_{\delta\tau}(\omega,\tau) = \frac{(e^{\delta\tau\,\omega}-1)^2(1+e^{(2\tau-\beta)\omega})}{e^{(\delta\tau+\tau)\omega}\,\delta\tau^2\,\omega^2}, \tag{A6}$$

in order to directly relate the quantum Monte Carlo estimator $C_{AB}(l\,\delta\tau)$ to $S_{AB}(\omega) = \int dt\, e^{i\omega t}\langle A(t)B\rangle$ corresponding to the real-time correlation function $\langle A(t)B\rangle$,

$$C_{AB}(l\,\delta\tau) = \int_0^\infty \frac{d\omega}{2\pi} K_{\delta\tau}(\omega,l\,\delta\tau) S_{AB}(\omega). \tag{A7}$$

This relation holds true without any approximation, irrespectively of the discretisation used in setting up the Monte Carlo estimator. The final inversion problem is then solved using e.g., the stochastic analytic continuation approach, with the kernel $K_{\delta\tau}(\omega,\tau)$ for the present case. As an example, we show in Fig. 12 the quantum Monte Carlo data for $S_B(\tau,\mathbf{k}) = \langle B_{\mathbf{k}}(\tau)B_{-\mathbf{k}}\rangle$ at the Γ point, $\mathbf{k} = 0$, and a coupling ratio of $g = 2.1$, along with the indicated asymptotic $1/\tau^4$ decay.

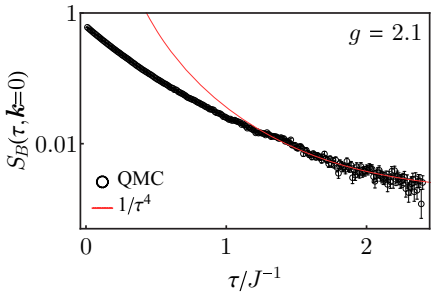

FIG. 12. (Color online) Imaginary-time (τ) dependence of $S_B(\tau,\mathbf{k}) = \langle B_{\mathbf{k}}(\tau)B_{-\mathbf{k}}\rangle$ at the Γ point, $\mathbf{k}=0$, for a coupling ratio of $g = 2.1$, along with an asymptotic $1/\tau^4$ decay, indicated by the line.

APPENDIX B: SPIN-WAVE THEORY

In this Appendix, we provide details on both the linear spin-wave theory calculations that we performed on the square-lattice bilayer as well as on the higher-order spin-wave theory approach that we used. In the classical limit of large spin S, the ground state of the Heisenberg model on the bipartite square lattice bilayer consists of an antiferromagnetic arrangement of the spins within and between the layers, irrespectively of the coupling ratio g. The classical spin structure can be parametrized by means of a single helix with pitch vector $\mathbf{Q} = (\pi,\pi,\pi)^{\intercal}$, such that for a spin on site l,

$$\mathbf{S}_l = S(0,0,e^{i\mathbf{Q}\cdot\mathbf{r}_l})\,. \tag{B1}$$

In this Appendix, the index l runs over all sites of the lattice, where $l = (i,\mu)$ is given by a rung index i plus a layer index μ, as in the main text. The quantum spin Hamiltonian is now rewritten expressing the spin operators in the local basis of the classical spin orientations, (x',y',z'),

$$\begin{aligned} S_l^x &= e^{i\mathbf{Q}\cdot\mathbf{r}_l} S_l^{x'}\,,\\ S_l^y &= S_l^{y'}\,,\\ S_l^z &= e^{i\mathbf{Q}\cdot\mathbf{r}_l} S_l^{z'}\,. \end{aligned} \tag{B2}$$

In this rotated frame, the classical ground state is thus ferromagnetic by construction.

1. Linear spin-wave theory

In the quantum model, the deviations from the classical order are expressed via the Holstein-Primakoff representation of spin operators [37]. To first order in $1/S$, the expressions take the form

$$\begin{aligned} S_l^{x'} &= \frac{\sqrt{2S}}{2}(a_l + a_l^\dagger)\,,\\ S_l^{y'} &= \frac{\sqrt{2S}}{2i}(a_l - a_l^\dagger)\,,\\ S_l^{z'} &= S - n_l\,, \end{aligned} \tag{B3}$$

with a_l ($a_l^\dagger$) local bosonic annihilation (creation) operators, and $n_l = a_l^\dagger a_l$. In this bosonic representation the expression of the quantum Hamiltonian, truncated at the harmonic order, takes the following compact form in Fourier space:

$$\begin{aligned} H = &-S(S+1)\left(2J + \frac{J'}{2}\right)N_S\\ &+ S\sum_{\mathbf{k}}(a_{\mathbf{k}}^\dagger, a_{-\mathbf{k}})\begin{pmatrix} A_{\mathbf{k}} & B_{\mathbf{k}}\\ B_{\mathbf{k}} & A_{\mathbf{k}}\end{pmatrix}\begin{pmatrix} a_{\mathbf{k}}\\ a_{-\mathbf{k}}^\dagger\end{pmatrix}, \end{aligned} \tag{B4}$$

where N_S is the total number of lattice sites, and the coefficients $A_{\mathbf{k}}$ and $B_{\mathbf{k}}$ are given by

$$\begin{aligned} A_{\mathbf{k}} &= 2J + \frac{J'}{2},\\ B_{\mathbf{k}} &= -J(\cos k_x + \cos k_y) - \frac{J'}{2}\cos k_z, \end{aligned} \tag{B5}$$

with $k_z = 0$ ($k_z = \pi$) for the symmetric (antisymmetric) sector. Terms of order S^2 in Eq. (B4) correspond to the classical energy and terms of order S to the $1/S$ correction. The quadratic Hamiltonian (B4) is diagonalized by introducing new bosonic quasiparticle operators via

$$\begin{aligned} a_{\mathbf{k}} &= u_{\mathbf{k}}\alpha_{\mathbf{k}} + v_{\mathbf{k}}\alpha_{-\mathbf{k}}^\dagger,\\ a_{\mathbf{k}}^\dagger &= u_{\mathbf{k}}\alpha_{\mathbf{k}}^\dagger + v_{\mathbf{k}}\alpha_{-\mathbf{k}}, \end{aligned} \tag{B6}$$

with $u_{\mathbf{k}}$ and $v_{\mathbf{k}}$ given by

$$\begin{aligned} u_{\mathbf{k}} &= -\mathrm{Sgn}(B_{\mathbf{k}})\left[\frac{1}{2}\left(\frac{A_{\mathbf{k}}}{\sqrt{A_{\mathbf{k}}^2 - B_{\mathbf{k}}^2}} + 1\right)\right]^{\frac{1}{2}},\\ v_{\mathbf{k}} &= \left[\frac{1}{2}\left(\frac{A_{\mathbf{k}}}{\sqrt{A_{\mathbf{k}}^2 - B_{\mathbf{k}}^2}} - 1\right)\right]^{\frac{1}{2}}. \end{aligned} \tag{B7}$$

The diagonal representation of H reads

$$H = -S(S+1)\left(2J_\parallel + \frac{J_\perp}{2}\right)N_S + \sum_{\mathbf{k}}\omega_{\mathbf{k}}\left(\alpha_{\mathbf{k}}^\dagger\alpha_{\mathbf{k}} + \frac{1}{2}\right), \tag{B8}$$

with the free magnon dispersion given by

$$\omega_{\mathbf{k}} = 2S\sqrt{A_{\mathbf{k}}^2 - B_{\mathbf{k}}^2}. \tag{B9}$$

The ground state of (B8) corresponds to the vacuum $|0\rangle$ of the Bogolyubov quasiparticles α and, for $S = 1/2$, we obtain a symmetric and an antisymmetric mode with dispersions

$$\begin{aligned} \omega_{(k_x,k_y,0)} &= 2J\sqrt{[1-\gamma(k_x,k_y)][1+\gamma(k_x,k_y)+g/2]},\\ \omega_{(k_x,k_y,\pi)} &= 2J\sqrt{[1+\gamma(k_x,k_y)][1-\gamma(k_x,k_y)+g/2]}, \end{aligned}$$

where

$$\gamma(k_x,k_y) = \tfrac{1}{2}(\cos k_x + \cos k_y), \tag{B10}$$

and $g = J'/J$. They satisfy the relation $\omega_{\mathbf{k}} = \omega_{\mathbf{k}+\mathbf{Q}}$, which implies that the dispersion of the symmetric and antisymmetric modes are identical up to a shift of the in-plane momentum by (π,π). The symmetric and antisymmetric modes soften respectively at $\mathbf{k} = 0$ and $\mathbf{k} = \mathbf{Q}$.

We next calculate the single-mode contribution to the dynamical spin structure factor in terms of the Bogolyubov

quasiparticles. To this end, we consider the operator

$$\begin{aligned} S^+_{\mathbf{k}} &= \frac{1}{\sqrt{N_S}} \sum_l e^{i\mathbf{k}\cdot\mathbf{r}_l} S^+_l \\ &= \frac{1}{\sqrt{N_S}} \sum_l e^{i\mathbf{k}\cdot\mathbf{r}_l} \left(e^{i\mathbf{Q}\cdot\mathbf{r}_l} S^{x'}_l + i S^{y'}_l \right) \\ &= \sqrt{\frac{S}{2}} (a_{\mathbf{k}} + a_{\mathbf{k}+\mathbf{Q}} + a^\dagger_{-\mathbf{k}-\mathbf{Q}} - a^\dagger_{-\mathbf{k}}). \end{aligned} \tag{B11}$$

In terms of the Bogolyubov quasiparticles, the effect of $S^+_{\mathbf{k}}$ onto the vacuum $|0\rangle$ is given by

$$S^+_{\mathbf{k}}|0\rangle = \sqrt{\frac{S}{2}} [(v_{\mathbf{k}} - u_{\mathbf{k}})\alpha^\dagger_{-\mathbf{k}} + (v_{\mathbf{k}+\mathbf{Q}} + u_{\mathbf{k}+\mathbf{Q}})\alpha^\dagger_{-\mathbf{k}-\mathbf{Q}}]|0\rangle, \tag{B12}$$

where we have used the property $u_{\mathbf{k}} = u_{-\mathbf{k}}$ and $v_{\mathbf{k}} = v_{-\mathbf{k}}$. Inserting Eq. (B12) into the Lehmann representation of the dynamical spin structure factor, and summing over the single-particle eigenstates of Eq. (B8) gives

$$S_S(\omega,\mathbf{k}) = \mathcal{Z}_S(\mathbf{k})\delta(\omega - \omega_{\mathbf{k}}), \tag{B13}$$

with the single-mode amplitude

$$\mathcal{Z}_S(\mathbf{k}) = \frac{S}{2}(|v_{\mathbf{k}} - u_{\mathbf{k}}|^2 + |v_{\mathbf{k}+\mathbf{Q}} + u_{\mathbf{k}+\mathbf{Q}}|^2), \tag{B14}$$

where we have used the identity $\omega_{\mathbf{k}} = \omega_{\mathbf{k}+\mathbf{Q}}$. Integrating $S_S(\omega,\mathbf{k})$ over ω yields the integrated spectral weight, $S_S(\mathbf{k})$, which within linear spin-wave theory in the single-particle sector is thus given by the single-mode amplitude $\mathcal{Z}_S(\mathbf{k})$. The integrated spectral weights for the symmetric and antisymmetric channels are thus given by

$$\mathcal{Z}_S(k_x,k_y,0) = \frac{4S^2 J(1-\gamma(k_x,k_y))}{\omega_{(k_x,k_y,0)}}, \tag{B15}$$

$$\mathcal{Z}_S(k_x,k_y,\pi) = \frac{4S^2 J(1-\gamma(k_x,k_y)+g/2)}{\omega_{(k_x,k_y,\pi)}}. \tag{B16}$$

Thus we recover the limiting behavior obtained numerically: the amplitude of the symmetric mode at $\mathbf{k} = 0$ vanishes linearly, while the amplitude of the antisymmetric mode at the antiferromagnetic Bragg peak position $\mathbf{k} = \mathbf{Q}$ diverges like $\sim 1/|\mathbf{k} - \mathbf{Q}|$, namely,

$$\mathcal{Z}_S(k,k,0) \approx \frac{JSk}{\sqrt{J(4J+J')}}, \quad k \to 0, \tag{B17}$$

$$\mathcal{Z}_S(k,k,\pi) \approx \frac{S\sqrt{J(4J+J')}}{J(k-\pi)}, \quad k \to \pi, \tag{B18}$$

respectively.

2. Higher-order spin-wave theory

As discussed in the main text, the agreement with the quantum Monte Carlo data is improved if the spin-wave expansion is extended beyond the harmonic order. The first step is to truncate the Holstein-Primakoff expansion to next-to-leading order. This amounts to keeping, in the expression of the spin operators in the rotated frame (x',y',z'), terms of order $S^{-1/2}$, such that

$$\begin{aligned} S^{x'}_l &= \frac{\sqrt{2S}}{2}(a_l + a^\dagger_l) - \frac{1}{4\sqrt{2S}}(n_l a_l + a^\dagger_l n_l), \\ S^{y'}_l &= \frac{\sqrt{2S}}{2i}(a_l - a^\dagger_l) - \frac{1}{4i\sqrt{2S}}(n_l a_l - a^\dagger_l n_l), \\ S^{z'}_l &= S - n_l . \end{aligned} \tag{B19}$$

Given the collinear nature of the classical state about which we perform the expansion, the terms beyond the usual harmonic contribution will be of quartic order in bosonic operators. To this level of approximation, we are left with a Hamiltonian

$$H = H^{(0)} + H^{(2)} + H^{(4)} + \mathcal{O}(1/S), \tag{B20}$$

where $H^{(0)}$, $H^{(2)}$, and $H^{(4)}$ are, respectively, the classical energy contribution $\sim S^2$, the harmonic fluctuation Hamiltonian $\sim S$, and the collection of all quartic interaction terms ~ 1. Lastly, $\mathcal{O}(1/S)$ denotes all the remaining terms in the expansion, which are of order $1/S^\alpha$ with $\alpha \geqslant 1$ and which we neglect. The expression for the sum $H^{(0)} + H^{(2)}$ is given in Eq. (B4), while $H^{(4)}$ is obtained as

$$\begin{aligned} H^{(4)} = &\frac{J}{2} \sum_{l,\mathbf{d}\in\{\pm\mathbf{x},\pm\mathbf{y}\}} \frac{1}{4}[(n_l + n_{l+\mathbf{d}})a_l a_{l+\mathbf{d}} + \text{H.c.}] - n_l n_{l+\mathbf{d}} \\ &+ \frac{J'}{4} \sum_{l,\mathbf{d}\in\{\pm\mathbf{z}\}} \frac{1}{4}[(n_l + n_{l+\mathbf{d}})a_l a_{l+\mathbf{d}} + \text{H.c.}] - n_l n_{l+\mathbf{d}} . \end{aligned}$$

To deal with this Hamiltonian, the simplest approximation consists in performing a mean-field decoupling of the quartic boson terms, and to evaluate the expectation values in the harmonic ground state. This yields an effective harmonic contribution $H^{(4)}_{\text{eff}} \sim 1$, which adds up to the quadratic terms $H^{(2)} \sim S$. Given the main objective of this calculation, which is just to demonstrate that the qualitative tendency is correct, we have not attempted to go beyond this simple treatment and to make the calculation of the expectation values self-consistent. This more sophisticated and significantly heavier approach, known as self-consistent spin-wave theory, includes higher-order corrections in an approximate way and would probably further improve the agreement, but it would anyway not allow to describe the quantum phase transition.

In Fourier space the sum $H_{\text{eff}} = H^{(0)} + H^{(2)} + H^{(4)}_{\text{eff}}$ has the same structure as Eq. (B4), with

$$\begin{aligned} H_{\text{eff}} = &-S(S+1)\left(2J + \frac{J'}{2}\right)N_S \\ &+ S\sum_{\mathbf{k}} (a^\dagger_{\mathbf{k}}, a_{-\mathbf{k}}) \begin{pmatrix} A^{\text{eff}}_{\mathbf{k}} & B^{\text{eff}}_{\mathbf{k}} \\ B^{\text{eff}}_{\mathbf{k}} & A^{\text{eff}}_{\mathbf{k}} \end{pmatrix} \begin{pmatrix} a_{\mathbf{k}} \\ a^\dagger_{-\mathbf{k}} \end{pmatrix} + \text{C}, \end{aligned}$$

where C is an additional constant of order $\mathcal{O}(1)$ and $A^{\text{eff}}_{\mathbf{k}}, B^{\text{eff}}_{\mathbf{k}}$ are the coefficients of Eq. (B5), evaluated at the effective couplings J_{eff} and J'_{eff} (i.e., $A^{\text{eff}}_{\mathbf{k}} = A_{\mathbf{k}}(J_{\text{eff}}, J'_{\text{eff}})$ and $B^{\text{eff}}_{\mathbf{k}} = B_{\mathbf{k}}(J_{\text{eff}}, J'_{\text{eff}})$), which are given by

$$J_{\text{eff}} = J\left(1 + \frac{\Delta - n}{S}\right), \quad J'_{\text{eff}} = J'\left(1 + \frac{\Delta' - n}{S}\right), \tag{B21}$$

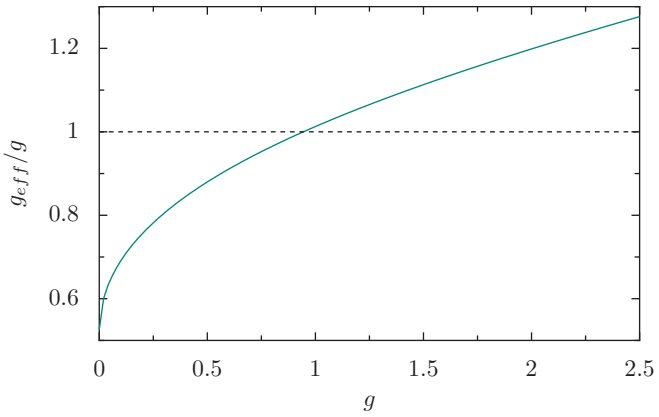

FIG. 13. (Color online) Effective coupling ratio $g_{\rm eff}$ as a function of g for $S = 1/2$.

where n, Δ, and Δ' are the following two-body averages computed in the harmonic approximation:

$$\begin{aligned} n &= \langle a_l^\dagger a_l \rangle, \\ \Delta &= \langle a_l\, a_{l+\mathbf{d}} \rangle \quad \text{for} \mathbf{d} \in \{\pm\mathbf{x}, \pm\mathbf{y}\}, \\ \Delta' &= \langle a_l\, a_{l+\mathbf{d}} \rangle \quad \text{for} \mathbf{d} \in \{\pm\mathbf{z}\}. \end{aligned} \tag{B22}$$

Note that all other two-body averages vanish, $\langle a_l^\dagger a_{l+\mathbf{d}} \rangle = 0$, and $\langle a_l\, a_l \rangle = 0$. The next-to-leading-order term of the spin-wave expansion thus has the effect of renormalizing the coupling ratio $g = J'/J$ via

$$g \longmapsto g_{\rm eff} = g\,\frac{S + \Delta' - n}{S + \Delta - n}\,. \tag{B23}$$

Depending on the values of the bare couplings J and J', the multiplicative coefficient ranges from values smaller than one to values bigger than one, as shown in Fig. 13. This figure suggests that for ratios $g \geqslant 1$, spin-wave interactions yield an effective ratio $g_{\rm eff}$ which is larger than the bare value. We conjecture that this renormalization will be even bigger if higher-order spin-wave interactions are taken into account. For example, we find that the quantum Monte Carlo results at $g = 2$ are rather well fitted by the spin-wave dispersion if the effective ratio, $g_{\rm eff}$, used is even larger than the one obtained from this improved spin-wave theory, as shown in Fig. 14. This figure also shows that for $g = 2.522$, an almost similarly good fit can be obtained.

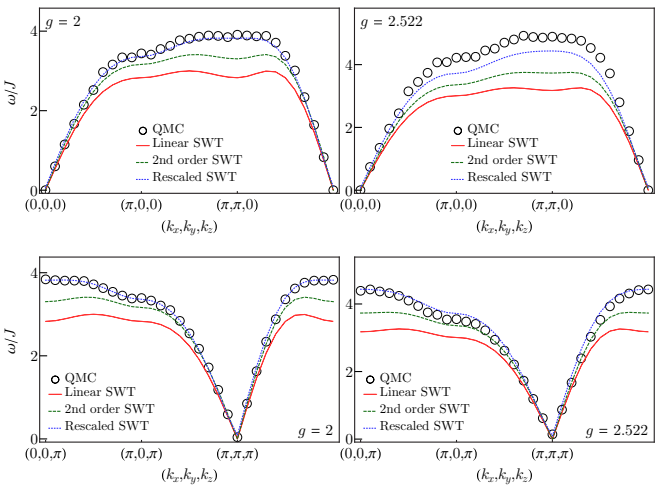

FIG. 14. (Color online) Plots of the dynamical spin structure factor at different ratios $g = J'/J$ inside the antiferromagnetically ordered region for the spin-half Heisenberg model on the square lattice bilayer. The panels compare the quantum Monte Carlo (QMC) results to both the linear and second-order spin-wave theory results as well as to further rescaled effective coupling ratios, which for $g = 2$ and 2.522 are obtained as $g_{\rm eff} = 1.8244g$ and $1.95g$, respectively.

APPENDIX C: PERTURBATION THEORY IN $1/g$

For vanishing intralayer coupling $J = 0$, i.e., in the limit $1/g = 0$, the ground state of the bilayer spin system is given by the direct product of singlets on the interlayer bonds (rungs). We denote this state by $|S\rangle = \bigotimes_i |s\rangle_i$, where $|s\rangle_i$ is the singlet on rung i,

$$|s\rangle_i = \frac{1}{\sqrt{2}}(|\uparrow\rangle_{i,1}|\downarrow\rangle_{i,2} - |\downarrow\rangle_{i,1}|\uparrow\rangle_{i,2})\,. \tag{C1}$$

To treat the intralayer coupling J as a weak perturbation in the small $1/g$ regime, we separate the total Hamiltonian H of the bilayer model in the interlayer and intralayer parts $H_\perp$ and $H_\parallel$, which scale respectively with J' and J. $|S\rangle$ is thus the ground state of $H_\perp$. Treating $H_\parallel$ as a weak perturbation to $H_\perp$, the ground state to first order in $1/g$ is found to be

$$\begin{aligned} |GS\rangle = |S\rangle - \frac{1}{4g} \sum_{i,\mathbf{d}\in\{\mathbf{x},\mathbf{y}\}} [&|t_0\rangle_i|t_0\rangle_{i+\mathbf{d}} \\ &- |t_1\rangle_i|t_{-1}\rangle_{i+\mathbf{d}} - |t_{-1}\rangle_i|t_1\rangle_{i+\mathbf{d}}]\,, \end{aligned} \tag{C2}$$

where the state $|t_n\rangle_i|t_m\rangle_{i+d}$ is the direct product of the triplets $|t_n\rangle$ and $|t_m\rangle$ on rungs i and $i + \mathbf{d}$ times the direct product of singlets on all other rungs (which are thus implicit in this notation). To study the dynamical spin structure factor, we consider the following local interlayer bond operators, which relate to the antisymmetric ($k_z = \pi$) and the symmetric ($k_z = 0$) modes:

$$S_i^{\rm AS} = \frac{1}{\sqrt{2}}(S_{i,1}^+ - S_{i,2}^+), \tag{C3}$$

$$S_i^{\rm S} = \frac{1}{\sqrt{2}}(S_{i,1}^+ + S_{i,2}^+). \tag{C4}$$

These operators act on the eigenstates of a rung as follows:

$$\begin{aligned} &S_i^{\rm AS}|s\rangle_i = -|t_1\rangle_i, \quad && S_i^{\rm S}|s\rangle_i = 0, \\ &S_i^{\rm AS}|t_1\rangle_i = 0, && S_i^{\rm S}|t_1\rangle_i = 0, \\ &S_i^{\rm AS}|t_0\rangle_i = 0, && S_i^{\rm S}|t_0\rangle_i = |t_1\rangle_i, \\ &S_i^{\rm AS}|t_{-1}\rangle_i = |s\rangle_i, && S_i^{\rm S}|t_{-1}\rangle_i = |t_0\rangle_i. \end{aligned} \tag{C5}$$

We first consider the antisymmetric sector. We start by computing the effect of

$$S_{\mathbf{k}}^{AS} = \frac{1}{\sqrt{N}} \sum_i S_i^{AS} e^{i\mathbf{k}\cdot\mathbf{r}_i} \tag{C6}$$

on the approximate ground state Eq. (C2) (where $\mathbf{k}$ is a two-dimensional vector and N is the number of interlayer bonds).

According to (C5) this operator promotes a singlet to a triplet, and thus the antisymmetric mode captures the dynamics of triplet excitations. Restricting ourselves to the single triplon sector, we obtain

$$S^{AS}_{\mathbf{k}}|GS\rangle = \left(-1+\frac{1}{g}\gamma(k_x,k_y)\right)|t_1\rangle_{\mathbf{k}}\,, \tag{C7}$$

with

$$|t_1\rangle_{\mathbf{k}} = \frac{1}{\sqrt{N}}\sum_i e^{i\mathbf{k}\cdot\mathbf{r}_i}|t_1\rangle_i\,, \tag{C8}$$

and $\gamma(k_x,k_y)$ defined in Eq. (B10). To compute the matrix elements entering the expression of the dynamical spin structure factor in the Lehmann representation, the knowledge of the full spectrum is required. Here, we will consider the perturbative eigenstates. Since we consider only the single triplet component of $S^{AS}_{\mathbf{k}}|GS\rangle$ (see Eq. (C7)), we can restrict ourselves to the eigenstates of the effective Hamiltonian

$$H^{\text{eff}} = H_\perp + P_1 H_\parallel P_1 + P_1 H_\parallel S H_\parallel P_1, \tag{C9}$$

where P_1 is the projector onto the single triplet degenerate manifold, and $S=(1-P_1)/(E_{1t}-H_\perp)$, E_{1t} denoting the energy of the single triplet degenerate manifold. The states $|t_1\rangle_{\mathbf{k}}$ are found to be eigenstates of H^{eff} with eigenvalues

$$H^{\text{eff}}|t_1\rangle_{\mathbf{k}} = \left[\left(-\frac{3}{4}J'N+J'\right)+2J\gamma(k_x,k_y) - \frac{J^2}{J'}\left(\frac{3}{4}(N-2)+\frac{1}{2}(4\gamma(k_x,k_y)^2-1)\right)\right]|t_1\rangle_{\mathbf{k}}\,. \tag{C10}$$

A similar calculation allows us to compute the ground-state energy to the same order in J/J',

$$E_0 = -\frac{3}{4}J'N - \frac{3}{4}\frac{J^2}{J'}N\,. \tag{C11}$$

Thus, overall we obtain for $\mathbf{k}=(k_x,k_y,\pi)^\intercal$, i.e., in the antisymmetric channel, the single-triplon contribution to the dynamical spin structure factor as

$$S_S(\omega,\mathbf{k}) = \mathcal{Z}_S(\mathbf{k})\delta(\omega-\omega_{\mathbf{k}})\,, \tag{C12}$$

with the spectral weight amplitude to first order in $1/g$ given by

$$\mathcal{Z}_S(\mathbf{k}) = 1-\frac{2}{g}\gamma(k_x,k_y)\,. \tag{C13}$$

The single triplon dispersion, correct up to quadratic order, is given by

$$\omega_{\mathbf{k}} = J'+2J\gamma(k_x,k_y)-2\frac{J^2}{J'}[\gamma(k_x,k_y)^2-1]\,. \tag{C14}$$

Equation (C13) shows that the amplitude of the dynamical spin structure factor for the antisymmetric mode is of order 1. The momentum modulations of the amplitude are an effect of order $1/g$, with the largest amplitude for $\mathbf{k}=(\pi,\pi,\pi)^\intercal$ and the lowest at $\mathbf{k}=(0,0,\pi)^\intercal$. These results compare well with the quantum Monte Carlo structure factor, as discussed in the main text (see Fig. 5).

Next, we turn to the calculation of the symmetric channel. We start by computing, for $\mathbf{k}=(k_x,k_y)^\intercal$, the effect of

$$S^S_{\mathbf{k}} = \frac{1}{\sqrt{N}}\sum_i S^S_i e^{i\mathbf{k}\cdot\mathbf{r}_i} \tag{C15}$$

on the approximate ground state in Eq. (C2). According to Eq. (C5), this operator cancels the singlet component of the wave function. The finite contributions come from the triplet component, and are of order $1/g$,

$$S^S_{\mathbf{k}}|GS\rangle = -\frac{1}{4g}\sum_{\mathbf{d}\in\{\mathbf{x},\mathbf{y}\}}(|t_1t_0\rangle_{\mathbf{k},\mathbf{d}}-|t_0t_1\rangle_{\mathbf{k},\mathbf{d}})(1-e^{i\mathbf{k}\cdot\mathbf{d}}), \tag{C16}$$

where we have introduced

$$|t_1t_0\rangle_{\mathbf{k},\mathbf{d}} = \frac{1}{\sqrt{N}}\sum_i e^{i\mathbf{k}\cdot\mathbf{r}_i}|t_1\rangle_i|t_0\rangle_{i+\mathbf{d}}\,, \tag{C17}$$

$$|t_0t_1\rangle_{\mathbf{k},\mathbf{d}} = \frac{1}{\sqrt{N}}\sum_i e^{i\mathbf{k}\cdot\mathbf{r}_i}|t_0\rangle_i|t_1\rangle_{i+\mathbf{d}}\,, \tag{C18}$$

the Fourier transforms of neighboring pairs of triplets with zero relative momenta. Similarly as before, to compute the matrix elements required for the dynamical spin structure factor, we will consider the perturbative eigenstates. Since, to order $1/g$, the states $S^S_{\mathbf{q}}|GS\rangle$ contain two triplets, $|t_0\rangle$ and $|t_1\rangle$, we can restrict the calculation to the eigenbasis of the effective Hamiltonian

$$H_2^{\text{eff}} = H_\perp + P_2 H_\parallel P_2, \tag{C19}$$

where P_2 is the projector onto the two triplet degenerate subspace. The effective Hamiltonian describes the two-body dynamics of two triplets ($|t_0\rangle$ and $|t_1\rangle$) in a sea of singlets. The full diagonalization of $H_\parallel$ inside the two-triplet sector is nontrivial, and we performed it numerically. We considered a $L=10$ lattice, yielding a two-triplet Hilbert space of dimension 9900. We performed a full diagonalization, resolving the energies in momentum space. The spectrum of H_2^{eff} forms a continuum in the thermodynamic limit; for our lattice size we have access to 100 values of the momentum in the whole Brillouin zone, and for each momentum, we get 99 eigenstates with different energies. The spectrum, with energies relative to the energy of the ground state, disperses around $2J'$, the energy cost of promoting two singlets into triplets. It is shown in Fig. 15. We do not obtain an explicit expression for the dynamical spin structure factor in the symmetric channel since

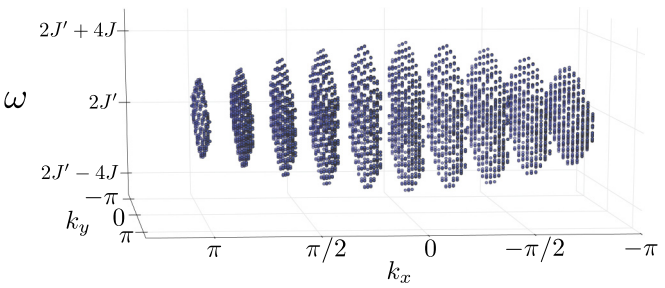

FIG. 15. (Color online) Spectrum of H_2^{eff} within the two-triplet sector for a system size $L=10$. Energies are measured with respect to the ground-state energy.

the eigenbasis and eigenenergies of $H_2^{\rm eff}$ are obtained only numerically. Instead, for each value of the momentum, we computed the overlap between $S^S_{\mathbf{k}}|GS\rangle$ and the eigenbasis of $H_2^{\rm eff}$. Thus, for each momentum, there is a distribution of amplitudes at different energies. This distribution of amplitudes is shown in Fig. 6 of the main text. Based on our analysis, a few remarks can be made about the dynamical spin structure factor associated to the symmetric mode: (i) it can be seen analytically that at zero momentum the amplitude of the dynamical spin structure factor in the symmetric channel vanishes (this may also be seen in Fig. 6). In fact, from Eq. (C16) one obtains $S^S_{\mathbf{k}=0}|GS\rangle = 0$. (ii) At momentum $\mathbf{k} = (\pi,\pi)^\intercal$, one can verify that $S^S_{\mathbf{k}=(\pi,\pi)^\intercal}|GS\rangle$ is an eigenstate of $H_2^{\rm eff}$ with energy equal to $2J' - J/2$ when counted from the energy of the groundstate. This explains why at $k = (\pi,\pi)^\intercal$ all the amplitude is concentrated at $\omega = 2J' - J/2$ in Fig. 6. (iii) The amplitude of the symmetric mode is of order $(1/g)^2$, while that of the antisymmetric mode is of order 1. Thus the signal of the symmetric mode vanishes in the limit $1/g \to 0$ (see Fig. 1).

APPENDIX D: BOND-BOND CORRELATIONS FROM THE $1/d$ EXPANSION

In this Appendix, we provide details of the calculation of the dispersion and the single-particle weight in the bond-bond correlations, which are related to the Higgs-peak contribution of the dynamical singlet structure factor $S_B(\omega,\mathbf{k})$, using the bond-operator-based $1/d$ expansion [42,43].

The starting point is a model of coupled dimers described by Eq. (1), but now on a hypercubic lattice in d spatial dimensions, such that the square-lattice bilayer corresponds to $d = 2$. To obtain a nontrivial large-d limit, it is crucial to properly scale the ratio between the interdimer coupling J' and the intradimer coupling J. To this end, we introduce the ratio

$$q = Jd/J' \tag{D1}$$

as our tuning parameter, with the notion that q is kept fixed upon taking the $d \to \infty$ limit. We refer the reader to Ref. [42] for an extended discussion of the $1/d$ expansion approach and the general formalism. In the following, we will restrict ourselves to $T = 0$ calculations. Further, most explicit expressions will be restricted to the leading order in $1/d$. Note that to this order (i.e., at the harmonic level) of approximation, the quantum critical point is located at $q = q_c = 1/2$.

As shown in detail in Refs. [42,43], the bond-operator approach yields a triply degenerate triplon (spin-1 excitation) mode in the quantum disordered phase (i.e., for $q < q_c$) while in the antiferromagnetically ordered phase (i.e., for $q > q_c$) one obtains two degenerate transverse modes (the Goldstone modes) and a longitudinal amplitude mode. In view of its further usage, we quote here the leading-order result [43] for the dispersion of the longitudinal mode (valid for $q \geqslant 1/2$):

$$\omega_{\mathbf{k},z} = 2J'q\sqrt{1 + \frac{\gamma_{\mathbf{k}}}{4q^2}}\,, \tag{D2}$$

where $\mathbf{k} = (k_1,k_2,\ldots,k_d)^\intercal$ and

$$\gamma_{\mathbf{k}} = \frac{1}{d}\sum_{i=1}^{d}\cos k_i\,. \tag{D3}$$

For the interlayer bond-bond correlations, we consider the susceptibility

$$\chi_B(\omega,\mathbf{k}) = -i\int_{-\infty}^{\infty} dt e^{i\omega t}\langle T_t B_{\mathbf{k}}(t)B_{-\mathbf{k}}(0)\rangle\,, \tag{D4}$$

where T_t is the time-ordering operator, and

$$B_i = \mathbf{S}_{i1}\cdot\mathbf{S}_{i2}\,, \tag{D5}$$

$$B_{\mathbf{k}} = \frac{1}{\sqrt{N}}\sum_i B_i e^{-i\mathbf{k}\cdot\mathbf{r}_i}\,. \tag{D6}$$

By the fluctuation-dissipation theorem, the imaginary part of the susceptibility χ_B is proportional to the structure factor S_B as considered in the main text. Expressed in terms of bond operators (we follow the notation of Ref. [42]), we obtain

$$B_i = \sum_{\alpha=x,y,z} t^\dagger_{i\alpha}t_{i\alpha} - \frac{3}{4}\,. \tag{D7}$$

In the disordered phase, the $t_{i\alpha}$ ($t^\dagger_{i\alpha}$) are annihilation (creation) operators for local spin-1 excitations, introduced within the bond-operator formulation. In the following, we work in the single-mode approximation (see Ref. [43] for details), i.e., we will ignore multimode contributions to the bond-bond correlation function which would cause continua in the spectrum. As a result, we neglect terms containing more than two triplon operators in the operator product $B_{\mathbf{k}}B_{-\mathbf{k}}$. We are then lead to the following expression for the interlayer bond susceptibility in the disordered phase:

$$\chi_B^{\rm dis}(\omega,\mathbf{k}) = N\big[\tfrac{9}{16} - \tfrac{9}{2}R_2 + \mathcal{O}(1/d^2)\big]\delta_{\mathbf{k},0}\delta(\omega)\,, \tag{D8}$$

where $R_2 = \langle t^\dagger_{i\alpha}t_{i\alpha}\rangle$ up to $\mathcal{O}(1/d)$. We thus do not obtain any spectral weight in this sector apart from a Bragg-like peak at $\omega = 0$. (We note that a two-triplon continuum appears at order $1/d$.)

In the ordered phase, we performed the calculations to leading order in $1/d$, i.e., at the harmonic level. Here, we use generalized triplon operators $\tilde{t}$ and $\tilde{t}^\dagger$, obtained from the t and $t^\dagger$ operators after a suitable rotation in Hilbert space [43]. Note that the $\tilde{t}_x$ and $\tilde{t}_y$ operators refer to the two degenerate transverse modes, while the $\tilde{t}_z$ operator corresponds to the longitudinal mode. Furthermore, we define the condensate parameter

$$\lambda = \sqrt{\frac{2q-1}{2q+1}}\,, \tag{D9}$$

corresponding to the condensation of one of the triplon modes in the ordered phase. We then obtain

$$\begin{aligned} B_i &= \mathbf{S}_{1i}\cdot\mathbf{S}_{2i} \\ &= -\frac{3}{4} + \tilde{t}^\dagger_{ix}\tilde{t}_{ix} + \tilde{t}^\dagger_{iy}\tilde{t}_{iy} \\ &\quad + \frac{1}{1+\lambda^2}[\tilde{t}^\dagger_{iz}\tilde{t}_{iz} + \lambda^2 P_i + \lambda e^{i\mathbf{Q}\cdot\mathbf{r}_i}(\tilde{t}^\dagger_{iz} + \tilde{t}_{iz})] \\ &= -\frac{3}{4} + \frac{\lambda^2}{1+\lambda^2} + \frac{\lambda}{1+\lambda^2}e^{i\mathbf{Q}\cdot\mathbf{r}_i}(\tilde{t}^\dagger_{iz} + \tilde{t}_{iz}) + \tilde{t}^\dagger_{iz}\tilde{t}_{iz} \\ &\quad + \frac{\tilde{t}^\dagger_{ix}\tilde{t}_{ix} + \tilde{t}^\dagger_{iy}\tilde{t}_{iy}}{1+\lambda^2}, \end{aligned} \tag{D10}$$

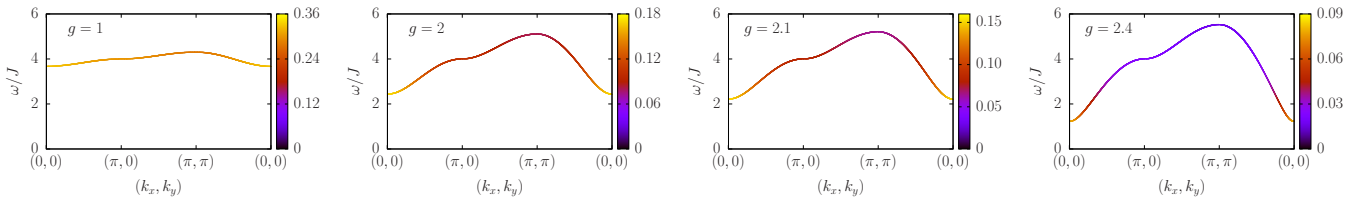

FIG. 16. (Color online) Spectral weight distribution in the dynamic singlet structure factor for different values of g, as obtained from the bond-operator theory using the mapping in Eq. (9).

where $\mathbf{Q} = (\pi,\pi,\dots)^{\intercal}$, and in the last equation, we have used the singlet projector $P_i = 1 - \sum_\alpha \tilde{t}^\dagger_{i\alpha}\tilde{t}_{i\alpha}$ (with $\alpha = x,y,z$). This gives

$$B_{\mathbf{k}} = \sqrt{N}\left(-\frac{3}{4} + \frac{\lambda^2}{1+\lambda^2}\right)\delta_{\mathbf{k},0} + \frac{\lambda}{1+\lambda^2}(\tilde{t}^\dagger_{\mathbf{k}-\mathbf{Q},z} + \tilde{t}_{-\mathbf{k}+\mathbf{Q},z}) + \frac{1}{\sqrt{N}}\sum_{\mathbf{q}}\left(\tilde{t}^\dagger_{\mathbf{q},z}\tilde{t}_{\mathbf{q}-\mathbf{k},z} + \frac{\tilde{t}^\dagger_{\mathbf{q},x}\tilde{t}_{\mathbf{q}-\mathbf{k},x} + \tilde{t}^\dagger_{\mathbf{q},y}\tilde{t}_{\mathbf{q}-\mathbf{k},y}}{1+\lambda^2}\right). \tag{D11}$$

As noted above, we now ignore the last term in the above equation since it will either contribute to the continuum or give a $1/d$ correction to the single-particle peak. Hence we do not obtain a single-mode contribution from the transverse modes. We are thus left with

$$\begin{aligned}\chi_B^{\mathrm{ord}}(\omega,\mathbf{k}+\mathbf{Q}) &= N\left(-\frac{3}{4} + \frac{\lambda^2}{1+\lambda^2}\right)^2\delta_{\mathbf{k},0}\delta(\omega) \\ &\quad + \frac{\lambda^2}{1+\lambda^2}[\mathcal{G}_{N,z}(\omega,\mathbf{k}) + \mathcal{G}_{N,z}(-\omega,\mathbf{k}) \\ &\quad + \mathcal{G}_{A,z}(\omega,\mathbf{k}) + \mathcal{G}_{A,z}(-\omega,\mathbf{k})] \\ &= N\left(-\frac{3}{4} + \frac{\lambda^2}{1+\lambda^2}\right)^2\delta_{\mathbf{k},0}\delta(\omega) \\ &\quad + \frac{\lambda^2}{1+\lambda^2}(u_{\mathbf{k},z} + v_{\mathbf{k},z})^2\left(\frac{1}{\omega-\omega_{\mathbf{k},z}} - \frac{1}{\omega+\omega_{\mathbf{k},z}}\right),\end{aligned} \tag{D12, D13}$$

where we have used the fact that $\mathbf{k}$ resides within the first Brillouin zone, and the fact that $\mathbf{k} \pm 2\mathbf{Q}$ is equivalent to $\mathbf{k}$. In the above expression, $\mathcal{G}_N$ and $\mathcal{G}_A$ denote the zero-temperature normal and anomalous Green's function, respectively. Also, $u_{\mathbf{k},z}$ and $v_{\mathbf{k},z}$ are Bogoliubov coefficients, used in diagonalising the Hamiltonian to leading order in $1/d$, and at this point we refer to Ref. [43] for their explicit expressions. We can now read-off the mode weight corresponding to $\omega_{\mathbf{k},z}$ from the above expression,

$$\mathcal{Z}_B(\mathbf{k}+\mathbf{Q}) = \frac{\lambda^2}{1+\lambda^2}(u_{\mathbf{k},z} + v_{\mathbf{k},z})^2 = \frac{2q-1}{2\sqrt{4q^2+\gamma_{\mathbf{k}}}}. \tag{D14}$$

As discussed in Sec. III, we need to account for the shift in the location of the quantum critical point within the bond-operator approach from the actual value, when comparing the above results to the quantum Monte Carlo data. In Fig. 16, we show the single-mode contribution to the spectral weight atop the corresponding dispersion relation for different values of g, using the mapping in Eq. (9) to the corresponding values of q used in the above formula. We recall that, in addition to this single-mode contribution, a two-magnon continuum appears at leading order in $1/d$, which we have not determined here. Finally, we note that within the current approach, one can similarly calculate the quasi-particle contribution to the bond-bond correlations among the intralayer bonds. Similar to the case of the spin-spin correlations, one can in this case distinguish between a symmetric and antisymmetric channel with respect to layer inversion symmetry. For the symmetric channel, we obtain again a single-mode contribution like in the interlayer case considered explicitly above, however, of reduced spectral weight. In the antisymmetric channel, no single-particle contribution is obtained so that only a continuum contribution results.

APPENDIX E: SPIN DYNAMICS IN THE HUBBARD MODEL

The bilayer Heisenberg model is an effective low energy model describing the spin dynamics of Mott insulators. In this appendix, we show that the spin dynamics obtained from simulations of the Heisenberg model can be obtained by starting from the Hubbard model on the bilayer square lattice. At intermediate couplings, this is by no means trivial since charge fluctuations allow for higher-order spin exchange processes. Our starting point is the Hamiltonian of the Hubbard model on the square lattice bilayer:

$$H = -\sum_{i,j,\sigma} c^\dagger_{i,\sigma} T_{i,j} c_{j,\sigma} + \frac{U}{2}\sum_i (n_i - 1)^2. \tag{E1}$$

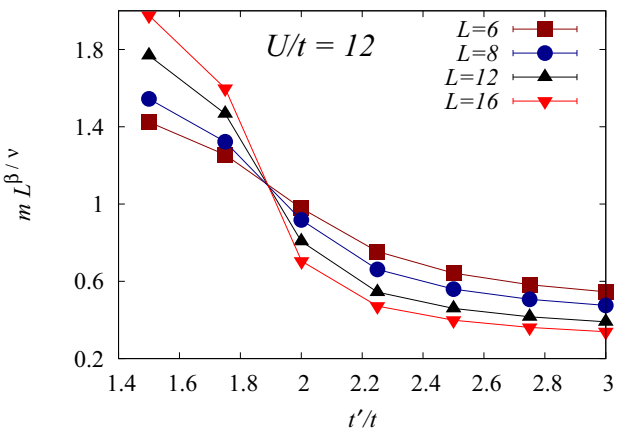

FIG. 17. (Color online) Finite size scaling of the staggered magnetization assuming 3D O(3) critical exponents [45], $\nu = 0.7048(30)$ and $\beta = 0.3616(31)$.

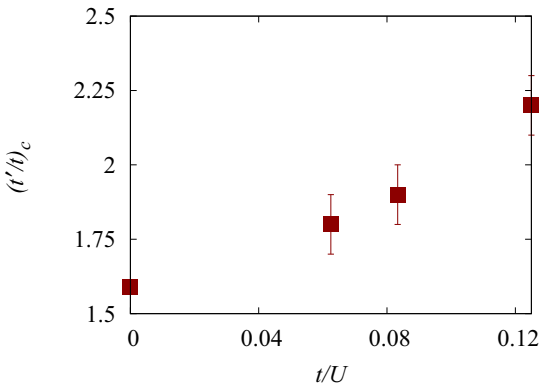

FIG. 18. (Color online) Critical value of t' as a function of the Hubbard interaction. The data point at $U/t \to \infty$ corresponds to the Heisenberg result.

Here, $c^\dagger_{i,\sigma}$ creates an electron in Wannier state centered around lattice site i and with z-component of spin σ, $T_{i,j}$ accounts for in-plane hopping of magnitude t between nearest neighbors as well as an interlayer hoping set by t'. Finally, double occupancy of Wannier states is prohibited by the Hubbad term, with $n_i = \sum_\sigma c^\dagger_{i,\sigma} c_{i,\sigma}$

At the particle-hole symmetric point, one can carry out sign-free quantum Monte Carlo simulations of the model. Here, we have used the projective zero-temperature approach based on the equation

$$\frac{\langle\Psi_0|O|\Psi_0\rangle}{\langle\Psi_0|\Psi_0\rangle} = \lim_{\Theta\to\infty} \frac{\langle\Psi_T|e^{-\Theta H} O e^{-\Theta H}|\Psi_T\rangle}{\langle\Psi_T|e^{-2\Theta H}|\Psi_T\rangle}, \tag{E2}$$

in which the ground state is filtered out of a single Slater determinant by propagating along the imaginary time axis. It is beyond the scope of this appendix to go into the details of the implementation and the reader is referred to Ref. [50] for an overview of the algorithm. Let us, however, comment on some aspects of our implementation. We have used an SU(2)-spin symmetric discrete Hubbard-Stratonovitch transformation, coupling to the charge:

$$e^{-\Delta\tau U(n_i-1)^2/2} = \frac{1}{2}\sum_{s=\pm1} e^{i\alpha s(n_i-1)}, \tag{E3}$$

with $\cos(\alpha) = e^{-\Delta\tau U/2}$. We have furthermore used a symmetric Trotter decomposition with $\Delta\tau U = 0.8$ and the trial wave function corresponds to the ground state of the noninteracting Hamiltonian. Here, parameters were chosen so as to avoid a degenerate ground state for the noninteracting system. Thereby, the trial wave function is a spin-singlet, and due to Liebs theorem [51] in the correct symmetry sector of the ground state of the bilayer Hubbard model. For this spin singlet trial wave function projection parameters $\Theta t = 40$ suffice to guarantee convergence to the ground state within the quoted accuracy.

In the strong-coupling limit, second-order perturbation in t/U yields $J = 4t^2/U$ and $J' = 4t'^2/U$ such that the Heisenberg result $g_c \equiv (J'/J)_c = 2.5220(1)$ translates to $(t'/t)_c = 1.59$ as $U/t \to \infty$. To determine the critical value of of t' for finite values of U, we have used the finite-size scaling ansatz:

$$m = L^{-\beta/\nu} F(|t'_c - t'|L^{1/\nu}) \tag{E4}$$

with the staggered magnetization

$$m = \sqrt{\langle \boldsymbol{S}_{\boldsymbol{Q}} \boldsymbol{S}_{-\boldsymbol{Q}}\rangle}. \tag{E5}$$

Here, $\boldsymbol{S}_{\boldsymbol{k}} = \sqrt{\frac{1}{N_s}}\sum_i e^{-i\boldsymbol{k}\cdot\boldsymbol{r}_i}\boldsymbol{S}_i$, with $\boldsymbol{S}_i = \frac{1}{2}\sum_{s,s'} c^\dagger_{i,s}\boldsymbol{\sigma}_{s,s'}c_{i,s'}$ the spin-1/2 operators, and $\boldsymbol{Q} = (\pi,\pi,\pi)$ the antiferromagnetic wave vector. Figure 17 shows the finite-size scaling of the staggered magnetization using the three-dimensional O(3) critical exponents [45]. As apparent, $(t'/t)_c = 1.9 \pm 0.1$ at $U/t = 12$. Similar results allow us to pin down the value of $(t'/t)_c$ as a function of U/t. The data, shown in Fig. 18, are consistent, as expected, with t'_c extrapolating to the Heisenberg value as $U/t \to \infty$. A similar analysis was recently carried out in Ref. [52].

To compare with the Heisenberg results, we have computed the dynamical spin structure factor, which in the Lehmann

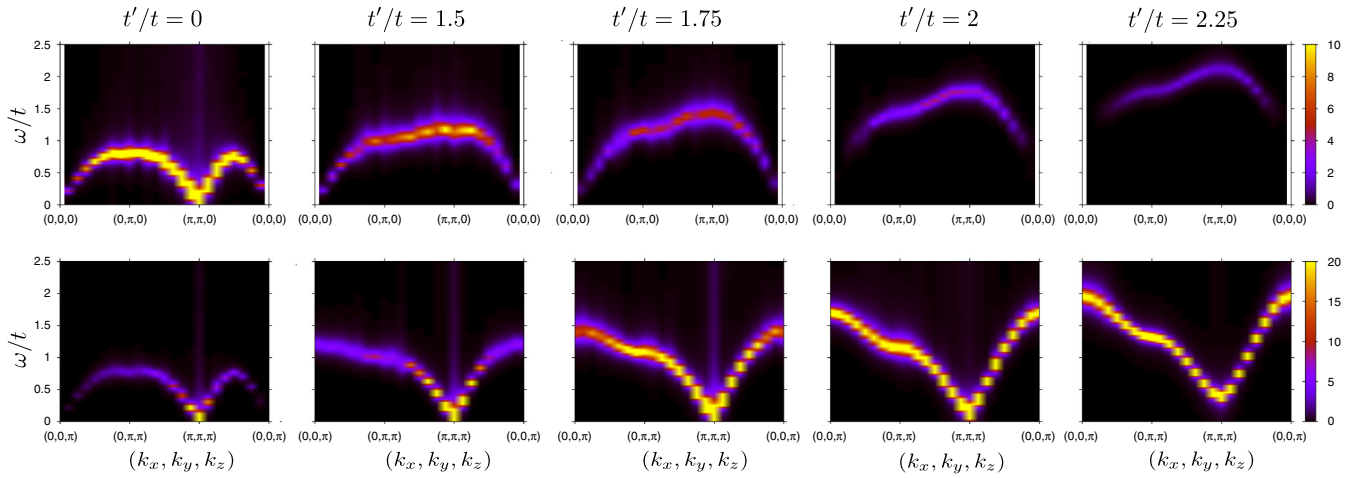

FIG. 19. (Color online) Dynamical spin structure factor at $U/t = 12$ across the quantum phase transition. For this value of the Hubbard interaction $(t'/t)_c = 1.9 \pm 0.1$. The numerical simulations were carried out with a spin singlet trial wave function.

representation reads

$$S_S(\omega,\boldsymbol{k}) = 2\pi \sum_n |\langle n|\boldsymbol{S}_{\boldsymbol{k}}|0\rangle|^2 \delta(\omega - E_n - E_0). \quad \text{(E6)}$$

The sum rule

$$\int d\omega S_S(\omega,\boldsymbol{k}) = 2\pi \langle \boldsymbol{S}_{\boldsymbol{k}} \cdot \boldsymbol{S}_{-\boldsymbol{k}} \rangle \quad \text{(E7)}$$

relates the static and dynamical spin structure factors. In analogy to the results produced for the Heisenberg model, we have used the stochastic analytical continuation described in Ref. [36] to carry out the Wick rotation.

Figure 19 shows the dynamical spin structure factor across the quantum phase transition at $U/t = 12$ on an $L = 16$ lattice. For this value of the U/t, the single-particle gap is of the order of $\Delta_s \simeq 4t$ such that the particle-hole continuum should become apparent as of $2\Delta_s \simeq 8t$. From the sum rule, it becomes apparent that the great majority of the spectral weight lies in magnon excitations. Comparison with Sec. III A shows that the overall evolution of dynamical spin structure factor is very similar, if not identical, to the QMC results for the Heisenberg bilayer.

[1] C. Ruegg, B. Normand, M. Matsumoto, A. Furrer, D. F. McMorrow, K. W. Kramer, H. U. Gudel, S. N. Gvasaliya, H. Mutka, and M. Boehm, Phys. Rev. Lett. **100**, 205701 (2008).

[2] P. Merchant, B. Normand, K. W. Krämer, M. Boehm, D. F. McMorrow, and Ch. Rüegg, Nat. Phys. **10**, 373 (2014).

[3] I. Affleck and G. F. Wellman, Phys. Rev. B **46**, 8934 (1992).

[4] It has been shown [L. Fritz, R. L. Doretto, S. Wessel, S. Wenzel, S. Burdin, and M. Vojta, Phys. Rev. B **83**, 174416 (2011)]; that coupled-dimer models in two space dimensions exhibit two distinct universality classes, one of standard O(3) Heisenberg character and one which features anomalously large corrections to scaling due to a nonclassical cubic interaction term.

[5] D. Podolsky, A. Auerbach, and D. P. Arovas, Phys. Rev. B **84**, 174522 (2011).

[6] D. Podolsky and S. Sachdev, Phys. Rev. B **86**, 054508 (2012).

[7] L. Pollet and N. V. Prokof'ev, Phys. Rev. Lett. **109**, 010401 (2012).

[8] K. Chen, L. Liu, Y. Deng, L. Pollet, and N. V. Prokof'ev, Phys. Rev. Lett. **110**, 170403 (2013).

[9] S. Gazit, D. Podolsky, and A. Auerbach, Phys. Rev. Lett. **110**, 140401 (2013).

[10] A. Rançon and N. Dupuis, Phys. Rev. B **89**, 180501(R) (2014).

[11] D. Pekker and C. M. Varma, Ann. Rev. Cond. Mat. Phys. **6**, 269 (2015).

[12] F. Rose, F. Léonard, and N. Dupuis, Phys. Rev. B **91**, 224501 (2015).

[13] S. A. Weidinger and W. Zwerger, Eur. Phys. J. B **88**, 237 (2015).

[14] M. Matsumoto, H. Kuroe, A. Oosawa, and R. Sekine, J. Phys. Soc. Jpn. **77**, 033702 (2008).

[15] M. Matsumoto, J. Phys. Soc. Jpn. **83**, 084704 (2014).

[16] W. Zwerger, Phys. Rev. Lett. **92**, 027203 (2004).

[17] R. R. P. Singh, M. P. Gelfand, and D. A. Huse, Phys. Rev. Lett. **61**, 2484 (1988).

[18] A. J. Millis and H. Monien, Phys. Rev. Lett. **71**, 210 (1993).

[19] A. J. Millis and H. Monien, Phys. Rev. B **50**, 16606 (1994).

[20] A. W. Sandvik and D. J. Scalapino, Phys. Rev. Lett. **72**, 2777 (1994).

[21] A. V. Chubukov and D. K. Morr, Phys. Rev. B **52**, 3521 (1995).

[22] T. Sommer, M. Vojta, and K. W. Becker, Eur. Phys. J. B **23**, 329 (2001).

[23] L. Wang, K. S. D. Beach, and A. W. Sandvik, Phys. Rev. B **73**, 014431 (2006).

[24] J. Helmes and S. Wessel, Phys. Rev. B **89**, 245120 (2014).

[25] C. J. Hamer, J. Oitmaa, and Z. Weihong, Phys. Rev. B **85**, 014432 (2012).

[26] By triplon, we mean an excitation, which is adiabatically connected to states with only one triplet dimer in a sea of singlet dimers in the limit of decoupled dimers (see Appendix C), by contrast to excitations which are adiabatically connected to states with more than one triplet dimer in the limit of decoupled dimers.

[27] Y. Sasago, K. Uchinokura, A. Zheludev, and G. Shirane, Phys. Rev. B **55**, 8357 (1997).

[28] M. Jaime, V. F. Correa, N. Harrison, C. D. Batista, N. Kawashima, Y. Kazuma, G. A. Jorge, R. Stein, I. Heinmaa, S. A. Zvyagin, Y. Sasago, and K. Uchinokura, Phys. Rev. Lett. **93**, 087203 (2004).

[29] S. E. Sebastian, N. Harrison, C. D. Batista, L. Balicas, M. Jaime, P. A. Sharma, N. Kawashima, and I. R. Fisher, Nature (London) **441**, 617 (2006).

[30] Jungho Kim, A. H. Said, D. Casa, M. H. Upton, T. Gog, M. Daghofer, G. Jackeli, J. van den Brink, G. Khaliullin, and B. J. Kim, Phys. Rev. Lett. **109**, 157402 (2012).

[31] M. Moretti Sala, V. Schnells, S. Boseggia, L. Simonelli, A. Al-Zein, J. G. Vale, L. Paolasini, E. C. Hunter, R. S. Perry, D. Prabhakaran, A. T. Boothroyd, M. Krisch, G. Monaco, H. M. Ronnow, D. F. McMorrow, and F. Mila, Phys. Rev. B **92**, 024405 (2015).

[32] A. W. Sandvik, Phys. Rev. B **59**, R14157 (1999).

[33] O. F. Syljuasen and A. W. Sandvik, Phys. Rev. E **66**, 046701 (2002).

[34] F. Alet, S. Wessel, and M. Troyer, Phys. Rev. E **71**, 036706 (2005).

[35] F. Michel and H. G. Evertz, arXiv:0705.0799; F. Michael, Ph.D. Thesis, University of Graz, 2007.

[36] K. S. D. Beach, arXiv:cond-mat/0403055.

[37] K. Yosida, *Theory of Magnetism*, Springer Series in Solid-State Sciences Vol. 122 (Springer-Verlag, Berlin, Heidelberg, 1996).

[38] S. Sachdev and R. N. Bhatt, Phys. Rev. B **41**, 9323 (1990).

[39] V. N. Kotov, O. Sushkov, Zheng Weihong, and J. Oitmaa, Phys. Rev. Lett. **80**, 5790 (1998).

[40] A. Collins, C. J. Hamer, and Zheng Weihong, Phys. Rev. B **74**, 144414 (2006).

[41] R. Ganesh, S. V. Isakov, and A. Paramekanti, Phys. Rev. B **84**, 214412 (2011).

[42] D. G. Joshi, K. Coester, K. P. Schmidt, and M. Vojta, Phys. Rev. B **91**, 094404 (2015).

[43] D. G. Joshi and M. Vojta, Phys. Rev. B **91**, 094405 (2015).
[44] A. Sen, H. Suwa, and A. W. Sandvik, Phys. Rev. B **92**, 195145 (2015).
[45] K. Chen, A. M. Ferrenberg, and D. P. Landau, Phys. Rev. B **48**, 3249 (1993).
[46] A. W. Sandvik and R. R. P. Singh, Phys. Rev. Lett. **86**, 528 (2001).
[47] M. Powalski, G. S. Uhrig, and K. P. Schmidt, Phys. Rev. Lett. **115**, 207202 (2015).
[48] M. Hasenbusch, J. Phys. A **34**, 8221 (2001).
[49] A. W. Sandvik, R. R. P. Singh, and D. K. Campbell, Phys. Rev. B **56**, 14510 (1997).
[50] F. Assaad and H. Evertz, in *Computational Many-Particle Physics*, edited by H. Fehske, R. Schneider, and A. Weiße, Lecture Notes in Physics Vol. 739 (Springer, Berlin Heidelberg, 2008), pp. 277–356.
[51] E. H. Lieb, Phys. Rev. Lett. **62**, 1201 (1989).
[52] M. Golor, T. Reckling, L. Classen, M. M. Scherer, and S. Wessel, Phys. Rev. B **90**, 195131 (2014).